Investigating the initial sodiation of silicon nitride conversion-type anodes for sodium-ion batteries

Bachelor Thesis Research

18/05/2026

Maastricht Science Program, Maastricht University.

Word count: 12816

Author: Marsal Colitt Marull (i6359826)

Project Supervisor: Dr. Emilia Olsson*

Internal Advisor: Dr. Jesse Hennekam**

*Advanced Research Center for Nanolithography (ARCNL), Science Park 106, 1098 XG Amsterdam; Institute of Theoretical Physics, University of Amsterdam, Science Park 904, 1098 XH Amsterdam

** Maastricht Science Program, Maastricht University. Paul-Henri Spaaklaan 1, 6229 EN Maastricht

Contents

ABSTRACT 3

1. INTRODUCTION 4

2. METHODS 9

2.1. Theoretical Background 9

2.2.1 Amorphous structure generation and sodium insertion 11

2.2.2 Sodium incorporation 12

3. RESULTS 13

3.1. Crystalline silicon nitride benchmarking 13

3.1.1. Sodium incorporation in crystalline silicon nitride 14

3.2. Amorphous characterization and selection of sodium insertion sites 16

3.3. Sodium insertion in amorphous silicon nitride 23

3.4 Sodium incorporation into silicon nitride 25

4. DISCUSSION 31

5. CONCLUSION 33

CRITICAL REFLECTION 34

APPENDIX 1 – CONVERGENCE TESTING 35

Basis set selection 35

Establishing supercell size 36

Cutoff and relative cutoff determination 36

APPENDIX 2 – COOLING RATE DETERMINATION 38

REFERENCES 41

ABSTRACT

The environmental impact of producing Li-ion batteries (LIBs) alongside the localized nature of Li-reserves has driven much attention towards LIB alternatives like Na-ion batteries (NIBs). A main hurdle in developing NIBs is in finding compatible anode materials. Recently, conversion-type anodes have gained traction, amongst which amorphous silicon nitride (a-Si_3N_4) has been shown to be a promising candidate, with capacities of up to 2000mAh/g in LIBs. Much work has been done in understanding the conversion rection of a-Si_3N_4 for LIBs, where an embedding matrix is formed, having been linked to the materials performance. For NIBs, this matrix formation process is largely still unknown. Here, the initial sodiation of a-Si_3N_4 was studied via atomic scale modelling, with a robust sampling scheme for Na site selection, developed to tackle the large variation in structural motifs present. A wide range of Na binding energies were found, largely dependent on coordination environment. Furthermore, we identified a strong correlation between sodium's interaction with nitrogen and incorporation energies, and postulated that the embedding matrix could form in a similar manner to the lithiation of a-Si_3N_4, providing important insights into the feasibility of a-Si_3N_4 as an anode material for NIBs.

1. INTRODUCTION

Be it through portable electronics, electric vehicles, or household appliances, few today can claim to have never used a battery. What's more, the importance of this technology is likely to increase in the future. Batteries are pivotal to the green energy transition. Sustainable production methods, such as solar and wind, rely on intermittent energy sources, often translating into irregular output levels.[8] Batteries go hand in hand with these new electricity production methods, allowing for energy storage during high production hours and discharge during production lows, catering to society's demand for a steady supply of electricity.[8]

Batteries rely on redox reactions, where an electrolyte separates the reduction and oxidations steps. Ions migrate through the electrolyte, from anode to cathode, whereas electrons are forced to go from one electrode to the other via an external circuit, producing electrical work (a).[3] Pivotal to any battery is that the discharge process be spontaneous. While charging, cations move from the cathode towards the anode, and an electron transfer occurs, producing neutral atoms that are stored in the anode. In the discharge process, however, once an external circuit is completed, the reverse electron transfer happens, where atoms spontaneously lose an electron and move towards the cathode, driven by a lower electrode potential.[9] The difference between the two electrode potentials is what defines the voltage of the electrochemical cell. In other words, a battery stores electricity as chemical energy, leveraging the fact that until the external circuit is completed the spontaneous reaction cannot occur.[9]

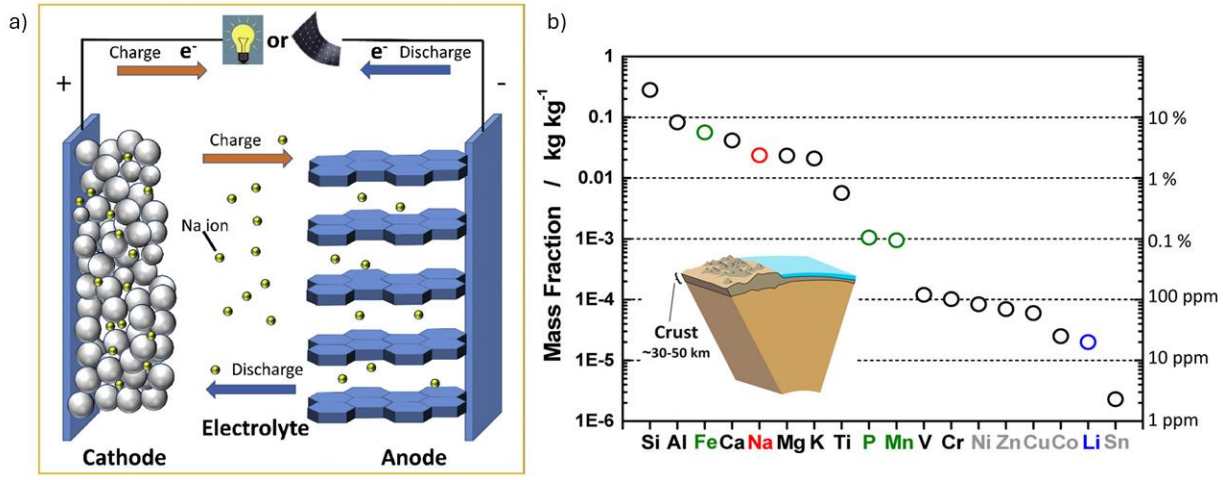

Figure 1 ***a)*** *Schematic diagram of working mechanism of sodium-ion battery*[5] *and* ***b)*** *mass fraction of common elements in the earth's crust.*[10]

A common measure of battery's storage capabilities is its capacity, in ampere-hours (Ah) or milliampere-hours (mAh), which, given a specified output current, is a product of said current and the discharge time of the battery at a given voltage.[9,11,12] Since current represents the rate at which charge flows, capacity is a measure of the total amount of electrical charge that can be stored in that battery.[12] In the battery literature, however, capacity density is often reported instead, in mAh/g, often just referred to as capacity.[1,3,11,13–16] Another closely related descriptor is energy density, reported in watt hours per kilogram (Wh/kg), where energy is the product of the capacity and the voltage.[11] Additionally, the lifespan of the battery also plays a vital role, with most batteries losing capacity over time, though some faster than others.[11] This is measured as the battery cycle-life and it is common to report how many charge/discharge cycles a specific capacity can be sustained for.[3,4,11,13,17]

The most widespread battery technologies are Li-ion batteries (LIBs), presenting revolutionary energy density levels upon their introduction, earning John B. Goodenough, M. Stanley Whittingham, and Akira Yoshino a Nobel prize in 2019.[18] Despite this, there is demand to complement these batteries with ones that can provide longer lifetimes, increased capacity, and greater safety.[1,3,19] Furthermore, the social and environmental impact of mining the resources required for LIBs, alongside the very localized nature of their reserves, helps drive this search (Figure 1b).[1,2] As an alternative to lithium, sodium has emerged as a viable contender.[13,20,21] Sodium is considerably more abundant, easier and cheaper to extract, and shares many electrochemical properties with lithium.[13] Despite compatible battery components struggling to keep up in development, sodium ion batteries (NIBs) have seen increased interest and are increasingly becoming commercially available, as highlighted in Figure 2.[5,20,21]

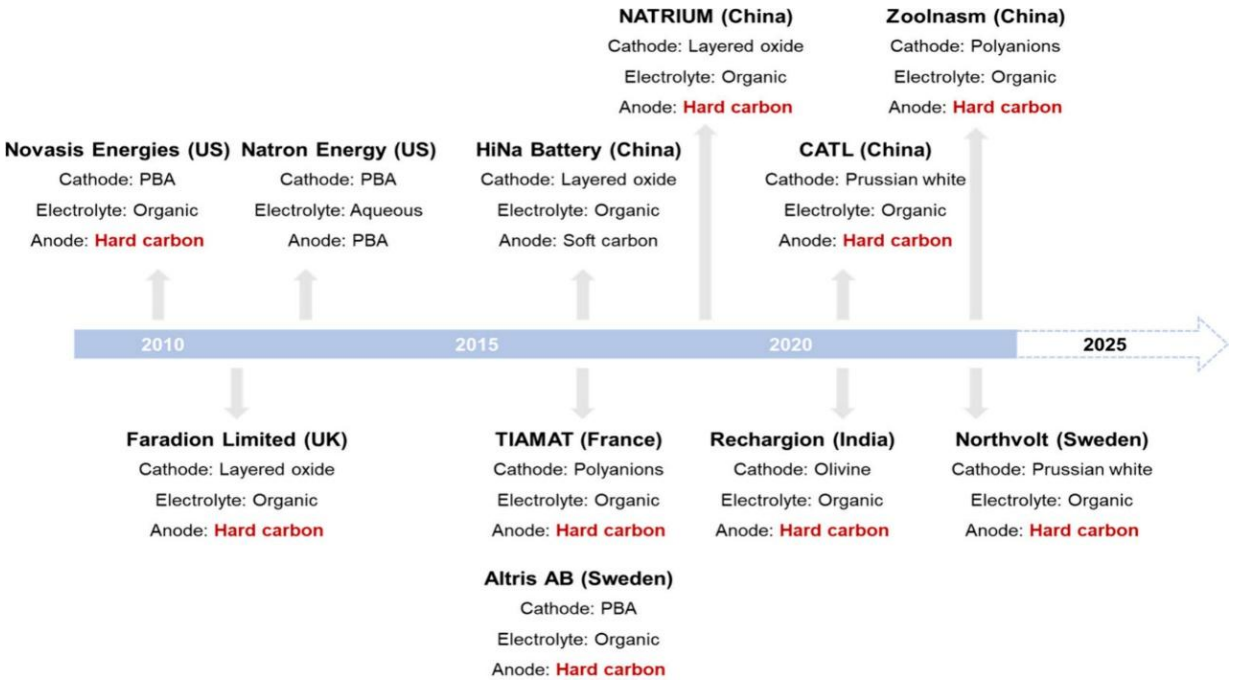

Figure 2. Recent progress in the commercialization of sodium-ion batteries.[20]

Another notable challenge in the search for higher performing materials is in increasing the anode capacity.[4] Currently, the most common LIB anode materials are of the intercalating type, where metal ions are reversibly stored in the host lattice with minimal changes to the structure.[6] Typically, this implies that these materials are mechanically stable, avoiding challenges relating to expansion of the lattice, but have limited ion storage sites.[3] Graphite, the most employed LIB intercalation type anode material, has a maximum capacity of 372 mAh/g for LIBs.[3] Though graphite has served LIBs well, and will continue to, the same cannot be said about NIBs, driving research towards hard carbon and alloy-type alternatives instead.[20] Sodium's larger ionic radius (1.02 Å vs 0.76 Å)[13] makes its incorporation thermodynamically unfavorable, leading graphite anodes for NIBs to have very low capacity, currently at 35 mAh/g.[22–24] This is shown in Figure 2 where, of the most notable instances of attempted NIB commercialization, all have opted for alternatives to graphite.

Comparatively, alloy-type anodes store ions quite differently to intercalating-types.[6] This class of anode materials undergo reversible alloying with the metal, allowing for increased ion storage, meaning higher theoretical capacities, but also often leading to large volume expansions upon charging. Silicon, the most studied alloy-type anode, has a high theoretical capacity of 3579 mAh/g in LIBs, but suffers from large lattice expansions of approximately 300%, making them impractical for many applications today.[4,14,15] In comparison to lithiation, there are few experimental studies on the sodiation process of silicon.[15] It is well known, however, that sodium suffers from a kinetically unfavorable Na-Si alloying process, leading to a far lower theoretical capacity, with one experiment reporting 340 mAh/g.[15,21]

The large volume increase of many alloy-type anodes, and the poor theoretical capacity of intercalation-type anodes, has brought much attention to conversion-type anodes as possible solutions for NIBs.[5,6] As the name suggests, these undergo a conversion of their structure to a different phase that involves an electrochemical redox reaction between two materials.[25] Tin-based amorphous oxides were the first presented conversion-type anodes, in 1997.[26,27] During the first charge cycle, these anodes typically undergo an irreversible conversion of their structure, assimilating some of the, drastically reducing the capacity of the cell after a few cycles.[26,28,29] Despite also facing contact issues with the changes in phase, potential volume expansions, and other obstacles, conversion-type anodes have had considerable breakthroughs and are an active field of research.[25]

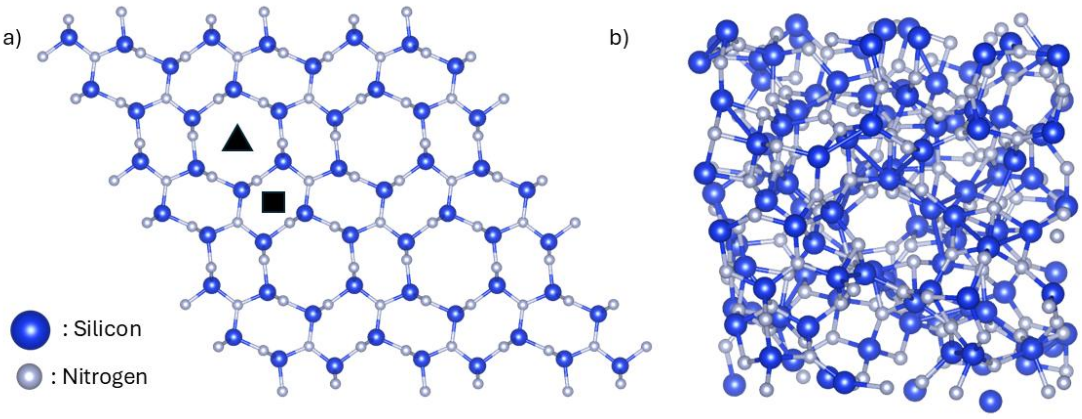

*Figure 3. Structures of **a)** β-Si_3N_4, with large channel indicated by a triangle and the small channel indicated by a square, and **b)** a-Si_3N_4.*

Lately, silicon nitride, Si_3N_4, has gained attention as a conversion-type anode, with reported capacities up to 2000 mAh/g for LIBs, in Si-rich stoichiometric ratios.[4] In crystalline form (Figure 3a), tetrahedral silicon is bonded to trigonal planar nitrogen atoms, forming large hexagonal channels (triangle in Figure 3a), surrounded themselves by six smaller channels (square in Figure 3a) in the β-phase. The material showcases interesting electronic properties and applications, in addition to displaying corrosion and shock resistance, and importantly, being easy to fabricate.[30,31] Martín-Gil *et al*. (2003)[32] were one of the first to assess the α-Si_3N_4 crystalline phase as a potential anode candidate for LIBs, motivated by the potential formation of the highly ionically conductive Li_3N structure. Results, nonetheless, stood at a disappointing capacity of 40 mAh/g, with stagnant progress in the following years.[33] More recently, however, there has been renewed

interest in the material, especially in the amorphous phase, a-Si_3N_4 (Figure 3b)[4–6,17,31] Though these configurations lose their translational symmetry, it is precisely the disorder in the structure that allows them to store an increased number of ions.[34]

Amorphous silicon nitride (a-Si_3N_4) has been studied both experimentally and theoretically.[4,17,28,35–38] Common defects in the non-crystalline structure include over-coordinated silicon and nitrogen atoms, with dangling bonds that can produce new electronic states.[36,37] There are also several intrinsic charge traps across the structure that originate as a result of the structure itself in the presence of an extra charge. The response of the structure to the presence of an extra electron is of importance to the search for new anode materials because during the discharge process, metal atoms can lose electrons to become cations. In a recent computational study, Hückmann *et al*. (2023)[35] categorized intrinsic charge traps in a-Si_3N_4, where electron traps were identified on either three-coordinated or fully-coordinated silicon atoms, causing bond angle distortions. In 65% of cases, the extra electron evoked deeper structural changes in the material as a response, elongating one of the silicon-nitrogen bonds to the point where the nitrogen is considered double-coordinated. In rare instances, the study found that the four coordinated silicon can share the extra electron with a neighboring silicon atom, forming a Si-Si bond.

In the recent interest in silicon nitride as an anode material, the effect that the degree of sub-stoichiometry has also been investigated.[4,17,28,39] Stoichiometric amorphous silicon nitride, a-Si_3N_4 or a-$SiN_{1.33}$, in fact, displays far lower capacity compared to silicon rich stoichiometric ratios in LIBs.[17] Ulvestad *et al*. (2018)[29] compiled known experimental outcomes and projected the specific capacity of silicon nitride in LIBs, after the first charge cycle, across a varying ratio of nitrogen to silicon (Figure 4). It is possible that the fact that silicon-rich ratios seem to deliver higher discharge capacities and lower irreversible capacity loss may be intrinsically linked to the material's initial conversion reaction. In a-Si_3N_4, the first lithiation cycle forms an electrochemically active phase that is rich in silicon, as well as an inert embedding matrix composed of lithiated nitridosilicates ($Li_xSi_yN_z$), in an irreversible process.[4,7] Significant efforts have been made to understand this matrix formation process, and its full composition.[4] Recently, Lovett *et al*. (2025)[7] proposed a shell model to describe the matrix, where a soft, inner Si core is formed, surrounded by a hard nitridosilicate shell that restricts the core's expansion. This is then suggested to account for the stable diameter of the core seen during cycling, whilst still allowing for high ionic conductivity, linking the increased electrochemical performance of the material to the matrix formation process. Also recently, Cottom *et al*. (2025)[4], taking an atomic-scale approach to the problem, proposed that the generation of the silicon-rich region is governed by the formation of polaron and bi-polaron trap states, inducing the structural changes.

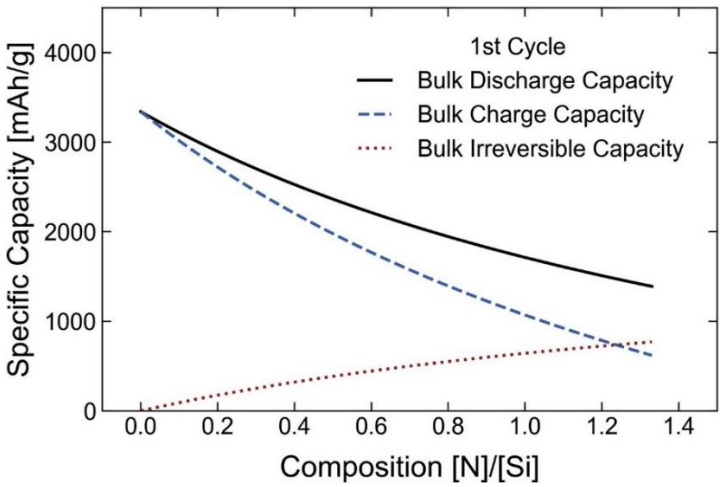

Figure 4. Predicted 1st cycle bulk discharge, charge and irreversible capacities of a-SiN_x as a function of nitrogen content.[40]

So far, the majority of scientific literature has focused on silicon nitride as an anode material for LIBs. The matrix formation process of silicon nitride in NIBs remains less studied, with some literature indirectly suggesting that the process may, in fact, be quite similar to that seen in LIBs. Damircheli *et al*. (2024)[41] used silicon nitride to form a more durable solid electrolyte interphase (SEI) layer for sodium-metal anodes. They found that an ionically conductive Na_3N layer formed, with silicon as a biproduct, similarly to what was thought for lithium in LIBs.[4,7] Furthermore, in the first recorded use of silicon nitride in NIBs, Cheng *et al*. (2021)[16] coated hard carbon with silicon nitride nanoparticles, at 7.9% by mass, and found that the anode's capacity increased from 284 to 351 mAh/g, compared to hard carbon without the coating. From the mass of silicon nitride used in their experiment, they then estimated a capacity of 848 mAh/g for an amorphous silicon nitride anode in NIBs, which, to date, has yet to be attempted. Interestingly, they also reported the formation of an amorphous silicon phase on the anodes, which as previously discussed, was found in the lithiation of a-Si_3N_4. Forming an atomic-scale understanding of the formation and more precise structure of this matrix is of great importance in elucidating the conversion mechanism of amorphous silicon nitride upon sodiation, moving this technology closer to commercial implementations. Addressing this is key to assessing the feasibility of silicon nitride as an anode for NIBs.

To address the matrix formation problem, computational methods offer many advantages, allowing for the probing of properties which, at that scale, are experimentally challenging, not to say impossible.[6,42] An atomic-scale modelling approach to the problem allows for deeper understanding of the underlying mechanisms that govern the experimental observations.[6,43] One example is sodium binding energies, also referred to as defect formation energies, where a positive formation energy indicates that the system is less thermodynamically stable than before the insertion. These are key for understanding whether it is energetically favorable for sodium ions (defects) to assimilate into an anode material. These binding energies can be linked to changes in structural motifs, which are crucial for the atomic-scale design of materials, whereby the computational results can guide experimental synthesis of materials, favoring structures that lead to more favorable binding energies.[6,44] Ultimately, it is also important that computational methods are capable of probing the electronic structure of the material.[45] Specifically, to look at the electronic response of the different structural motifs and sodium binding sites.

In this thesis, driven in part by sodium's similar electrochemical properties to lithium and the increased attention towards silicon nitride as an anode material, we study the atomic-scale structural evolution upon first sodiation of a-Si_3N_4. Insights into how sodium changes the coordination geometry of the amorphous structure, involving average bond lengths and angles, as well as incorporation energies and changes to the electronic structure are probed with density functional theory (DFT). Sodium binding sites are systematically categorized with a developed statistical sampling scheme, and the specific geometric motifs that lead to trends in binding energies are explored. This work provides important insights into the matrix formation process in a-Si_3N_4 upon sodiation.

2. METHODS

2.1. Theoretical Background

To conduct an atomic-scale study of the sodium incorporation in amorphous silicon nitride, Density Functional Theory (DFT) was employed. DFT is an electronic structure method, based on the existence of a functional that takes in the electron density at a point and outputs the energy at that point, instead of having to input three spatial coordinates for each electron in the system.[46] Though this electron density is not known before hand, one can get closer to the "true" electron density and, therefore, closer to the true energy at that point, which can be extrapolated to the entire system, allowing one to study the effect of atomic positions on specific properties of interest.[46] These are known as cell optimizations, where a step involves shifting the atomic positions and lattice vectors, and re-calculating the system's energy at that point.[46,47] The aim is then to find the set of atomic positions and lattice constants that minimize the energy of the system.[46,47] This can also be described as allowing the system to relax to its lowest energy state. Geometry optimizations can be considered a subset of these, where lattice parameters are kept constant but atomic positions are allowed to change. Before running DFT calculations, the energy cutoff and relative energy cutoff need to be adjusted to ensure energy conversion of the system.

To generate amorphous structures, molecular dynamics (MD), another type of computational methodthat updates atomic positions over time using Newton's, classical laws of motion, can be used.[46–49] At each time step, interatomic forces are calculated, based on which, current velocities and positions are updated to give new ones that are then update in the next time step, in an iterative process.[47,49] Contrary to DFT, the interaction between atoms is not directly calculated from quantum mechanical principles at every step.[48] Instead, a force-field is derived, without explicit inclusion of any electrons, that defines the potential energy of the system based on atomic positions.[49] This drastically reduces the computational cost of these simulations and allows for large systems to be studied. MD simulations can be carried out under many thermodynamic conditions, with properties like temperature, energy, volume, pressure, and number of atoms, having the freedom of being held constant or allowed to vary.[47–49] MD simulations can run on the timescale of nanoseconds, which orders of magnitude longer than what current DFT methods are capable of.[50] This makes it ideal for generating the amorphous structures, as these require simulating large ensembles under constant and varying temperatures for longer periods of time.

2.2. Computational Methods

To study the insertion of sodium atoms into the amorphous system, a multi-stage methodology was developed, an overview of which can be found in Figure 5. Firstly, convergence testing took place, followed by Na insertions into crystalline silicon nitride, in order to contextualize the results from the amorphous structure. Following this, amorphous structures were generated, and a robust sampling scheme was developed to statistically analyze the complex coordination environment and select appropriate sites. Subsequently, sodium atoms were inserted into the amorphous structure, after which an analysis of their effect on the structure was made. Visualizations of crystalline and amorphous structures were made using the VESTA (v. 3.90.5a)[51] and VMD (v. 2.0.0)[52] software packages.

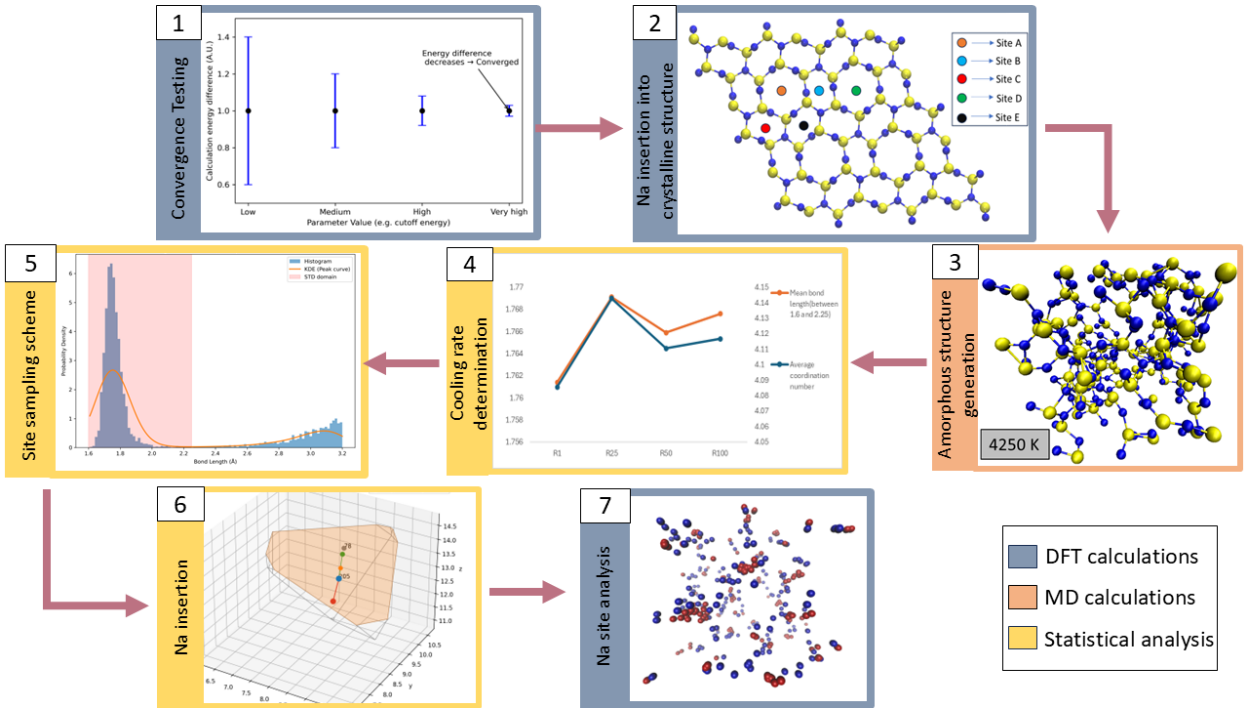

Figure 5. Schematic overview of the general methodology used in this investigation.

DFT calculations took place within the quantum chemistry and solid-state physics CP2K open-source software (v.2023.1 and v.2024.3)[53], which performs well with large lattices. Following convergence testing (Figure 5, step 1), four integration grids were used with a cutoff of 600 Ry for the finest one and a relative cutoff of 70 Ry. Furthermore, for β-Si_3N_4 crystalline structure, the supercell dimensions were also converged, resulting in the use of a 3x3x3 supercell. The DZVP-MOLOPT-SR[54] basis set was used with GTH[55–57] pseudopotentials to reduce the computational cost of the core electrons. Further explanation and results for the convergence process can be found in Appendix 1. Spin restriction was not applied to any calculations. Finally, geometry optimizations were performed using the BFGS[58] algorithm and the self-consistent field (SCF) convergence criteria set at a difference in energy of 10^{-7} eV between steps. The computational settings described were used with the PBE[59] functional. For four specific models, in order to

achieve increased accuracy, all settings, except for an increase in cutoff to 650 Ry and the use of the HSE06[60,61] exchange-correlation functional, were kept the same. In addition, for certain structural motifs, detailed in the results section 3.1.1 and 3.4, the electronic structure of the system was probed with a density of states (DOS) calculation, that gives an estimate of how many electronic states there are at each energy, around the Fermi energy level, and in particular, in the area under the valence band maximum (VBM) and above the conduction band minimum (CBM).[62] The total DOS can be split up into the particular contributions that each element's atomic orbitals have, known as the partial density of states (PDOS). Because of this, the specific location of the sodium states can be seen and what the most likely acceptor states in the conduction band (CB) are. Finally, in DOS plots the band gap, which corresponds to the difference between the energy of the CBM and VBM, can be identified.[62]

Crystalline structures were studied with a DFT cell optimization of the β-Si_3N_4 cell (Figure 5, step 2). Once optimized, sodium was placed in the small and large channels present in the structure, and the system was allowed to relax with constant lattice vectors. Long range interactions were then assessed by placing multiple sodium atoms in each channel, as well as in adjacent channels, to sufficiently sample the crystalline environment.

2.2.1 Amorphous structure generation and sodium insertion

Amorphous structures were generated (Figure 5, step 3), via a melt quench procedure using MD, as is typically done in computational studies.[35,48,63,64] Melt quenching involves heating a material until it is molten and then rapidly cooling it down, which prevents it from settling into the lowest energy conformation - a crystal, forming instead an amorphous network of atoms that are kinetically, but not thermodynamically stable.[65] MD simulations were run in the LAMMPS software (v. 29 Aug 2024)[66] using the MG2[67] interatomic potential, under an isothermal-isobaric ensemble. The lack of long-term order in amorphous structures make it isotropic, and so to avoid spurious interactions, cubic boxes are typically used.[48] For this, γ-Si_3N_4 was chosen as the starting structure, and a 224 atom supercell was constructed. The melting temperature was set at 4250 K, which is when the root mean square displacement of atoms reached a full cell length and there were no remnants or crystal motifs left. The cooling rate was set at 1K/ps (Figure 5, step 4), determined via a statistical analysis of the average bond lengths and coordination numbers, an explanation of which can be found in Appendix 2. Because the temperature here is finite, the way in which velocities are partitioned can be changed. Here, ten boxes were generated via a different partitioning of these velocities based on a random seed, meaning that each melt quench run started from a different place. Once the runs start, however, they equilibrate to the same high temperature, and quench at the same rate. However, since the starting positions were different, we are then left with ten different amorphous models, each containing 224 atoms.

An important question to ask before inserting sodium ions into the amorphous structure is where to place them. One of the main challenges associated with this is that a systematic sampling method, representative of the diverse configurational landscape present in the amorphous structure, relies on some form of site description or characterization. Because amorphous structures lack the repeating motifs of a crystal, determining which and how many sites in the amorphous boxes need to be sampled must be a statistical decision. In other words, a method is required to determine what percentage of sites need to be sampled, to obtain results that are representative of the whole structure (Figure 5, step 5). Determining this site sampling

scheme formed a large part of this investigation and the process is extensively discussed in the results section 3.2.

To determine what an appropriate number of sites to be sampled is, a large sample size is desired, for which all sites in the 10 boxes generated via the melt quench were considered. However, to ensure a higher degree of accuracy, an HSE optimization of the boxes is desired. Due to their increased computational cost, these were provided by the hosting research group, where the same melt quench parameters were used. A total of four boxes were selected for the insertion of sodium atoms, each representative of a specific silicon nitride electron trap site, and each containing 280 atoms. With this, the effect that the inserted sodium atoms have on these trap sites, as well as on the structure of amorphous silicon nitride itself. The site selection scheme developed with the larger sample size was then applied to each of the four HSE optimized boxes separately (Figure 5, step 6). Each selected site was sampled individually, in its own cell, generating many initial geometries, all of which were subsequently allowed to relax.

2.2.2 Sodium incorporation

Once the DFT optimizations of all the simulation boxes were completed, defect formation energies or sodium binding energies, E_{form}, were calculated based on the formalism of Zhang and Northrup, using equation 1.[4,68] Though the equation was developed to calculate the energy of defects within a network, in order to emphasize that Na insertion is intentional and is not seen as a defect in the structure, the terms defect formation energy, binding energy, and incorporation energy can be used interchangeably.

$$E_{form} = \frac{E_{nNa:Si_3N_4} - E_{Si_3N_4} - n\mu_{Na}}{n} \quad (1)$$

Here, $E_{Si_3N_4}$ is the total energy of the cell, and $E_{nNa:Si_3N_4}$, the total energy of the same cell with n inserted sodium ions. μ_{Na} is the chemical potential of sodium, which can take on different values depending on how the element is found. Sodium's lowest energy state is as bulk sodium. However, atomic sodium could also be considered, and their difference, calculated using the same level of theory described in the computational parameters section, is of approximately 1.17 eV/atom. In a battery, however, sodium is neither in a bulk state nor a free atom in a vacuum, and its true chemical potential is likely somewhere in between, depending on the electrolyte solution used.[11] Binding energies reported in the following sections are referenced to sodium's lowest energy state, but it is important to be mindful of the physical relevance of each. Equation 1 was used to calculate binding energies of sodium insertion in both crystalline and amorphous structures (Figure 5, step 7).

3. RESULTS

3.1. Crystalline silicon nitride benchmarking

As a starting point, crystalline lattice parameters were optimized via a cell optimization of a 3x3x3 β-Si_3N_4 supercell. Results and literature comparisons are summarized in Table 1. Lattice vectors were found to show good agreement with previous computational studies and similar discrepancies between computational and experimental studies were seen. Mean bond lengths were in line with experimental data, and with slight discrepancies with computational studies, though these report a wide range of results.[30] Lastly, the band gap for the crystalline structure was determined to be 4.27 eV, in good accordance with other computational studies, as shown in the PDoS plot (Figure 6). The valence band (VB) was found to be dominated by nitrogen p states, and the CB, mostly dominated by silicon p states, especially near the CBM.

Table 1. Lattice constants (A, B, and C), mean bond length, and band gap found in this investigation, as well as results from two computational studies, and an experimental one.

Parameter		This work	Computational (PBE)[67]	Computational (PBE)[68]	Experimental[69]
Lattice constants (Å)	A, B	7.648	7.665	7.647	7.609
	C	2.940	2.927	2.915	2.908
Mean bond length (Å)		1.748	1.816	-	1.734
Band gap (eV)		4.27	4.4 4.26 (HSE-06)	-	-

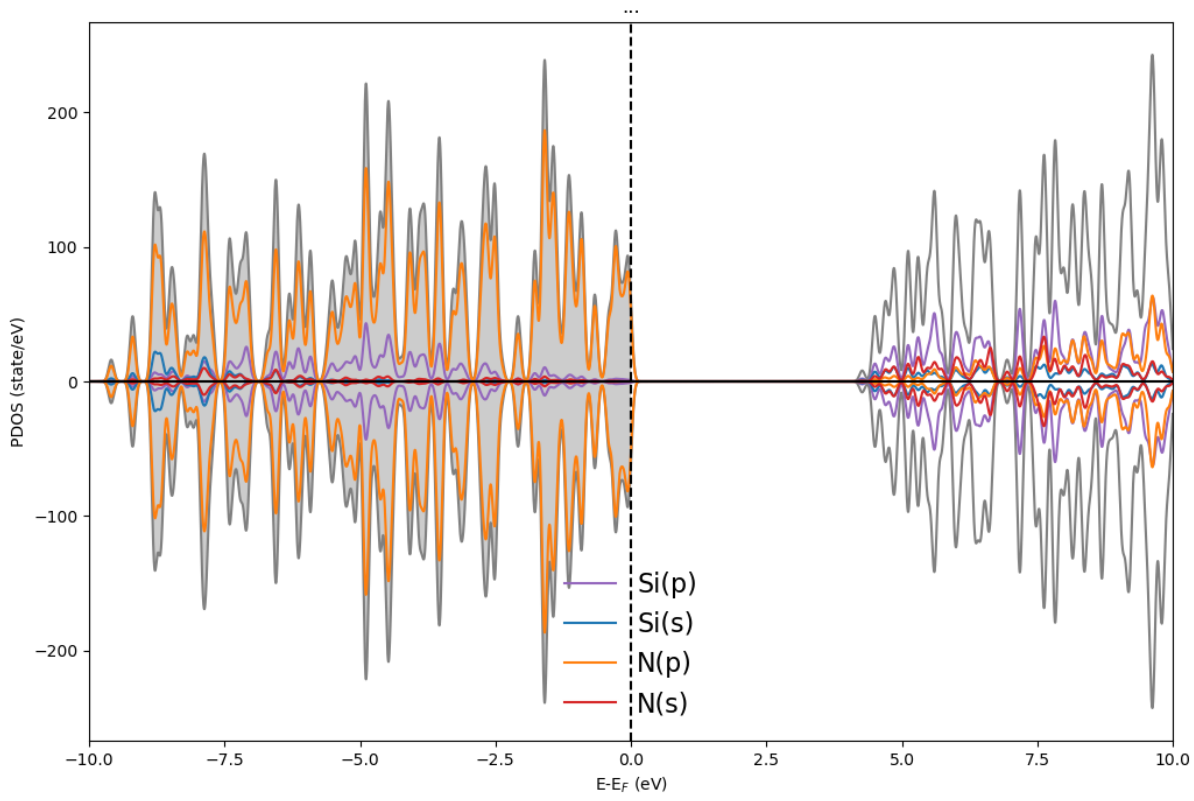

Figure 6. PDoS plot of β-Si3N4, with gray shaded areas demonstrating occupation.

3.1.1. Sodium incorporation in crystalline silicon nitride

To study the energetic stability of Na incorporation in crystalline Si_3N_4, sodium ions were subsequently inserted into the optimized crystalline structure, at unique symmetry insertion sites labeled A through E in Figure 7. For single insertions, through symmetry, sites A and D are equivalent (large channel), as well as sites B, C and E (small channel). Sodium incorporation energy for the large channel site was found to be 2.34 eV, with the sodium relaxing to occupy a position in the center of the channel, in phase with the rings forming the channel, and maximizing distance from the surrounding atoms. This is similar to what was found for the lithiation of the larger channel (2.37 eV)[4]. For the small channels, a significantly less favorable binding energy of 7.69 eV were calculated, whereas the same site had a binding energy of 4.56 eV for lithiation. The drastic increase in energy between the two sites is likely linked to the fact that the largest space inside the small channel is no wider than 3.4 Å, which is smaller than sodium's covalent diameter, causing severe electrostatic repulsion and structural deformation upon relaxation. Sodium's larger size can also be used to explain the larger discrepancy seen with the lithiation of the small channel.

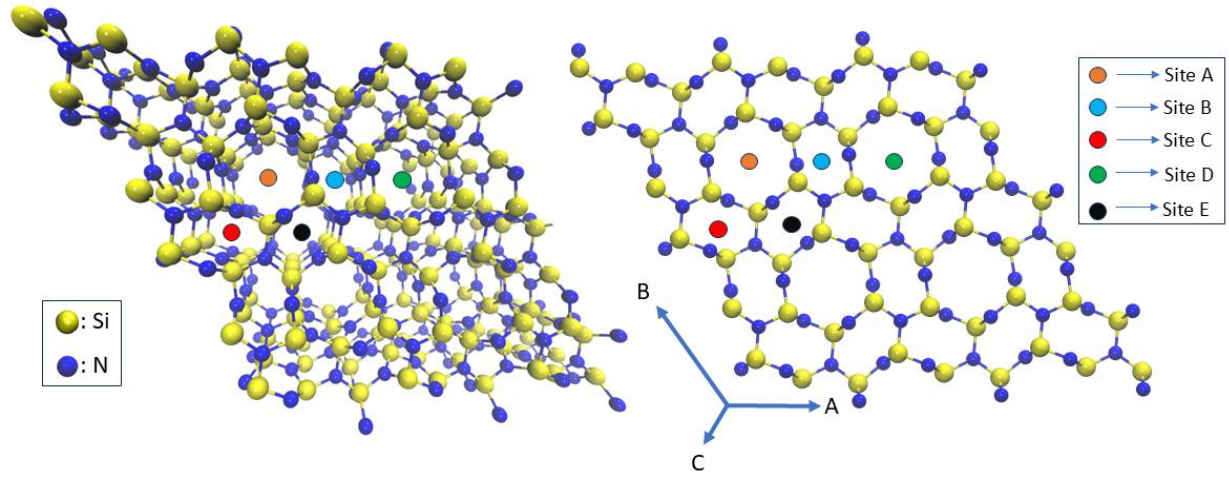

Figure 7. Perspective view (left) and orthographic view (right) of β-Si_3N_4 along shortest cell axis (C). Sodium insertion sites are represented by colored dots on the structure and translated to site labels in the legend (top right).

Shifting attention to multiple sodium insertions, two and three sodium were inserted into large channels, individually, allowing for an increased sampling of the crystalline environment. The atoms were placed along the ring sites in the channel, two rings apart, so as to not induce steric repulsion. Formation energies for the large channel increased marginally to 2.41 and 2.69 eV per atom, respectively. The two sodium atoms stabilized at 3.6 Å from each other, and 5.22 Å from the following sodium. The increase in energy for the double sodium insertion is likely caused by an increase in local lattice distortion, and the following insertion then causing steric effects between the sodium atoms. To assess long range interactions between the sodium atoms in the large channels, two sodium were inserted at sites A and D simultaneously, and found to result in an energy increase compared to individual sodium insertions was less than 0.02 eV, leading to the conclusion that there is little or no interaction between sodium atoms in the large channels at these concentrations.

Two sodium atoms were also placed in the small channel, where a decrease in binding energy to 6.40 eV per atom was seen. These relaxed at 2.73 Å from one another. Under certain conditions, Na can form a dimer, which could lower the energy of the system. However, the reported calculated bond length for this dimer varies between 3.08[69] Å and 3.57[70] Å, and would likely not account for the 1.29 eV difference between the two insertions. To further evaluate the interaction between the sodium atoms in the small channels, sites C and E (two adjacent small channels), and sites C and B (two small channels, one channel apart) were sampled. This clearly shows that having the sodium atoms close to each other reduces the systems energy compared to individual insertions, with energy increase for simultaneous insertion into sites C and E, having a sodium binding energy of 6.68 eV, and C and B, an energy of 7.208 eV. However, relaxed sodium atoms at sites C and B are over 6 Å apart, making any wavefunction overlap, and therefore, any bonding near impossible. What was seen instead, however, is that the channel in between the insertion sites experiences similar strain from the two atoms on opposite sides, minimizing the lattice distortion, and likely contributing to the lower energy seen, in comparison to individual insertions into those same sites.

Lastly, the PDOS of both the large and the small channel single insertions (sites A and E, respectively), were calculated and plotted around the CBM (Figure 8). It was seen that the band gap remained unchanged (Figure 6) in both cases and was unaffected by the sodium insertions. Both DOS plots showed a sodium states approximately 1 eV into the conduction band. Furthermore, it can be seen that the sodium atom formed a sodium ion, evidenced by the single occupied, spin up, state at the CBM, in both cases.

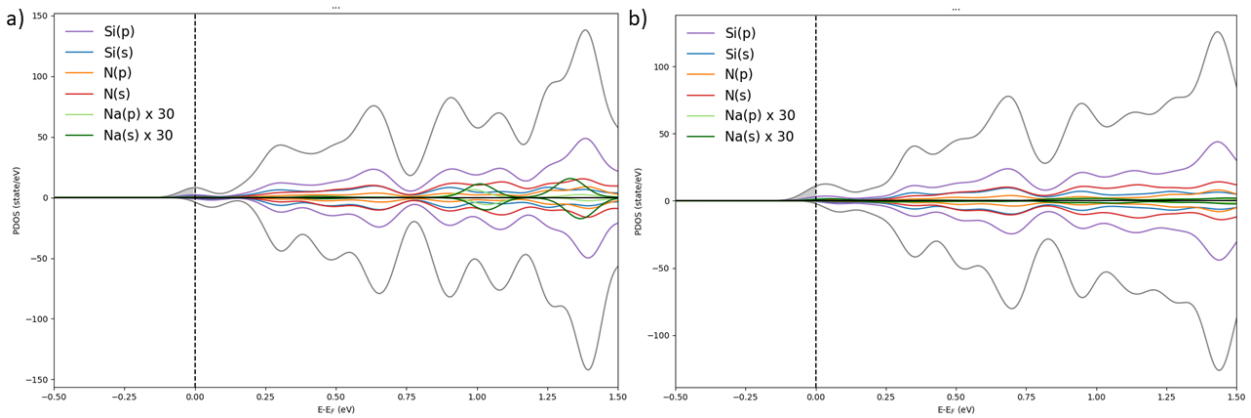

*Figure 8. Zoomed in PDOS around the CBM, with sodium states amplified by a factor of 30 to increase visualization, and gray shaded areas demonstrating occupation, of β-Si3N4 with **a)** a sodium insertion at site A in Figure 7 (large channel) and **b)** a sodium insertion at site E in Figure 7 (small channel).*

In general, the weak binding energies seen for both the small and large channels show an unfavorable incorporation of sodium into the structure. Though the insertions were not tremendously impactful towards the electronic structure of the system, the geometric distortions resulting from large electrostatic repulsions show that β-Si_3N_4 is an unsuitable anode material for NIBs, as was seen by Martín-Gil, et al. (2003)[32]. Having shown the infeasibility of the crystalline structure, amorphous structures were next generated, statistically analyzed, and sampled.

3.2. Amorphous characterization and selection of sodium insertion sites

In order to determine what the response of a-Si_3N_4 is to the insertion of sodium atoms, we must first ensure that the sampled sites are representative of the whole structure. That is, we must ascertain how many sodium atoms to insert and where to insert them. For this, a sampling scheme was developed that takes into account the large variation in environments present within the structure. Though the basic repeating motifs of a crystalline system are missing in an amorphous structure, local order can be maintained. This means that a metric such as coordination number (CN) can serve as an early sorting method in categorizing the available sampling sites. This was the starting point of the developed sampling scheme, an overview of which is shown in Figure 9. As mentioned in the methods section (Section 2.2.1), all bond lengths and bond angles and the data analysis originating therefrom, were compiled over the 10 replicates produced during the melt quench, each containing 224 atoms, to have as large of a dataset as possible on which to base the sampling scheme.

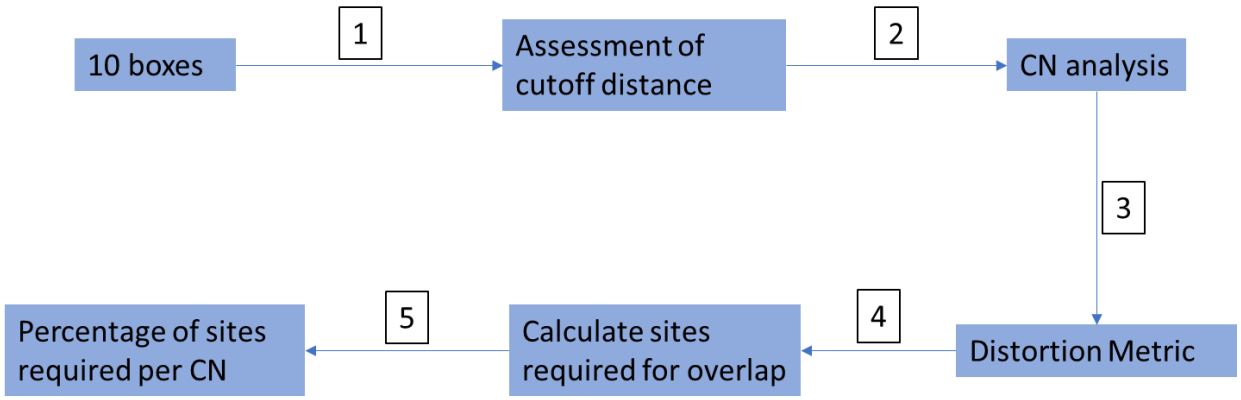

Figure 9. Flowchart showcasing the overview of the here developed sampling scheme.

Investigating the coordination number for an amorphous structure involves first determining what to be considered a bond. That is, a certain cutoff distance needs to be determined that delimits the coordination sphere. In other words, when looking at how many atoms are surrounding each nitrogen or silicon atom, we must first determine at which distance from the nitrogen or silicon atom to look for neighboring atoms. For this, the distances of all pairs of bonds were calculated using a pair-distribution function (PDF) (equation 2).[71] The function is normalized and describes the probability, for a given atom, of finding another atom, a certain distance, r, away.[71]

$$g_2(r) = \frac{V}{N^2}\left\langle \sum_{ij} \frac{\delta(r_{ij}-r)}{4\pi r^2} \right\rangle \quad (2)$$

Here, r_{ij} represents the distance between atom i and atom j. The bracketed sum represents taking the average over the entire ensemble. The function is also normalized, with N representing the number of atoms in the system and V, the system's volume, whereby as the distance from any given atom, r, approaches infinity, the probability of finding an atom, $g_2(r)$, approaches 1.

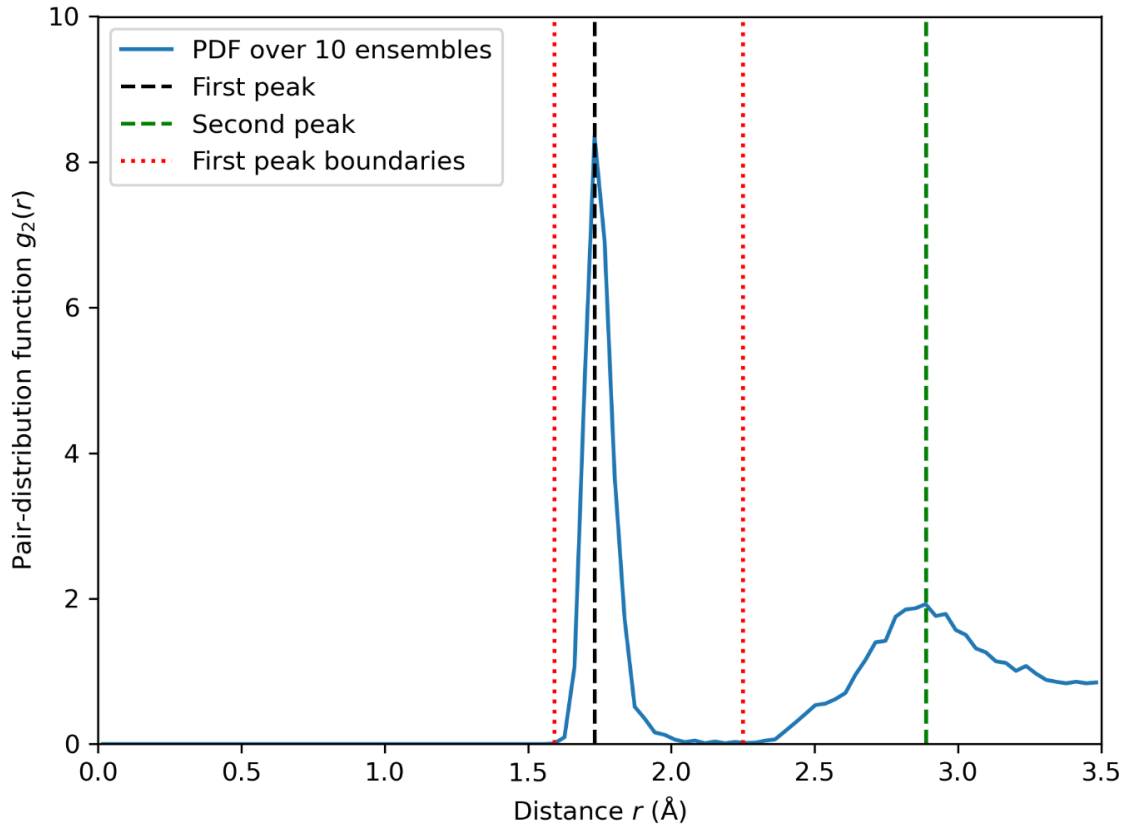

Figure 10. Pair-distribution function (blue) averaged over the ten melt-quench ensembles, with peak lines (black and green) set at local maxima and peak boundaries (red), set on the left where $g_2(r)$ reaches zero, and on the right at the last point before the $g_2(r)$ begins increasing again.

The first coordination shell of an atom contains the atoms that are directly bonded to the center atom, or first-neighbors. The second coordination shell of a center atom includes the first-neighboring atoms, but also the atoms bonded to the first neighbors, known as second-neighbors. The PDF plot (Figure 10) shows a first and second coordination shell present, with peak maxima at 1.73 Å and 2.89 Å, respectively. The first coordination shell cutoff was found to be 2.25 Å, set where the last minimum occurs before the start of the second peak. Once this cutoff point was determined, average bond lengths were calculated and found to be approximately 1.76 Å for the amorphous silicon nitride structures, in good agreement with both computational[30,36] and experimental data[72]. The average bond length found is approximately 0.1 Å longer than what was seen in the crystalline system, indicating that, on average, local geometry is well maintained in the amorphous system. With the cutoff selected, a coordination sphere was then constructed for every atom, inside which, any atom was considered bonded to the center atom (Figure 9, step 2). Since the material is composed of two different elements, which are prone to different coordination geometries and numbers, silicon's and nitrogen's coordination numbers were analyzed separately. There were no instances of N-N bonds or Si-Si bonds found, and therefore, all coordination reported is strictly Si-N bound, which is expected and indicates that no artifacts were introduced into the structure. Tallied coordination numbers across all replicates are shown in Table 2.

Table 2. CN number tally and frequency for silicon and nitrogen, over all replicates.

Si	**CN**	**3**	**4**	**5**	**6**
	Sites	2	877	78	3
	Frequency (%)	0.21	91.35	8.13	0.31
N	**CN**	**2**	**3**	**4**	
	Site tally	52	1094	134	
	Frequency (%)	4.06	85.47	10.47	

The average coordination number for silicon and nitrogen was found to be 4.09 and 3.06, respectively. These value are larger than previous computational studies (3.97 and 2.87, respectively)[35]. This indicates that the models constructed with the melt-quench procedure described in the methods section of this investigation are, on average, marginally over-coordinated instead of the literature reported slight under-coordination. On one hand, this is likely due to the reported literature values being calculated at the HSE level of theory, which tend to improve local descriptions compared to the MG2 classical potentials used which are better for average network descriptions.[50] On the other hand, the data found in reference 35 was obtained by forcing isotropy onto the calculated boxes, which is expected to produce a larger number of defects. In reality, there is likely an interplay between the two, with the latter having a slightly smaller influence on the difference in obtained results.

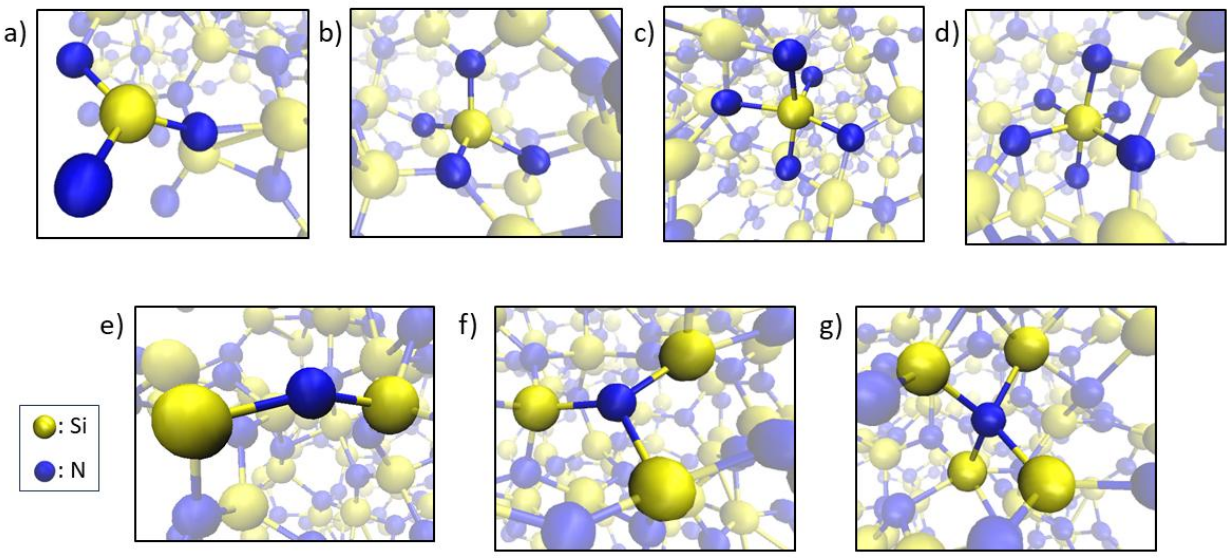

*Figure 11. Various geometries found in the amorphous structure depicting **a)** three-coordinated Si, **b)** four-coordinated Si, **c)** five-coordinated Si, **d)** six-coordinated Si, **e)** two-coordinated N, **f)** three-coordinated N, **g)** four-coordinated N.*

Figure 11 shows an overview of the different kinds of identified coordination geometries in the amorphous structures. For silicon, the three-coordinated sites all show the same geometry - a slightly distorted trigonal planar structure (Figure 11a). The same is observed for the six-coordinated silicon sites (Figure 11d), where all three sites have a slightly distorted octahedral structure. Within the five-coordinated silicon sites (Figure 11c), two categories of structures were observed, trigonal bipyramidal and square pyramidal, though for many of the sites a geometry in between the former and the latter was seen. Lastly, composing the large majority of Si sites, the four-coordinated (Figure 11b) were all found to resemble a tetrahedral geometry, with a large range of bond angles. For the nitrogen sites, the two-coordinated sites formed a bent structure (Figure 11e), with an angle that displayed a wide range across the different sites, from 90° to 173°, and an average angle of 140°. Similar to silicon, the three-coordinated nitrogen sites formed trigonal planar geometries (Figure 11f), composing most of the sites. Lastly, the four-coordinated nitrogen sites (Figure 11g) formed tetrahedrons that had a higher degree of distortion than the ones found for silicon.

shows the distribution of bond angles for the most frequently occurring coordination numbers for each element. As highlighted above, not all sites for a specific coordination number follow a precise geometry with consistent bond angles and lengths, as is expected for an amorphous structure. Figure 12a, depicts four-coordinated Si with a fairly even distribution around the ideal angle. This is contrasted by the five-coordinated sites (Figure 12b), where many sites take on a geometry in between trigonal bipyramidal and square planar, resulting in a chaotic, non-symmetric distribution of bond angles, varying from site to site. This non-symmetric distribution is also seen for the nitrogen sites (Figures 12c and 12d). In the context of this sampling method, however, this means that the variation in the sites needs to be taken into account.

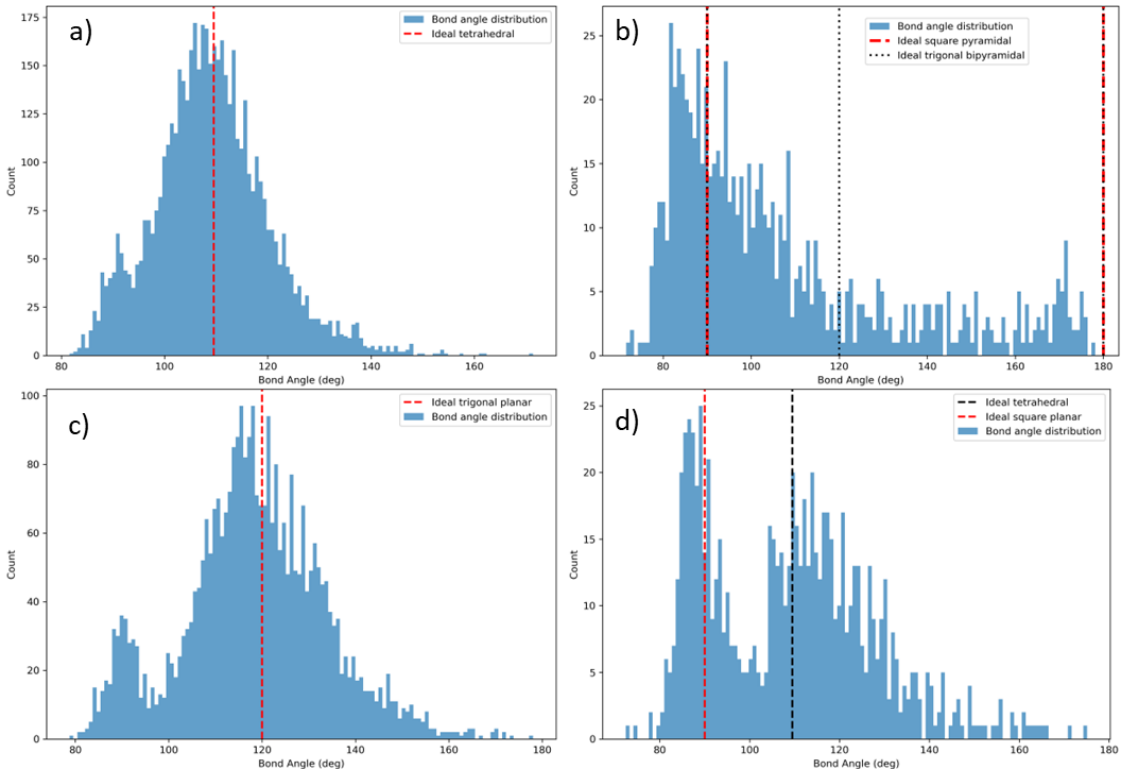

*Figure 12. Bond angle distributions for **a)** four- and **b)** five-coordinated silicon, and **c)** for three- and **d)** four-coordinated nitrogen.*

Now that each site is given an appropriate coordination number, the next question becomes how many sites for each coordination number must be sampled in order to obtain results that are statistically representative of the structure as a whole. This question is intrinsically linked to how different the sites within a given coordination shell are. In other words, we want to assign each site a score of how disordered it is. To illustrate this method, let us consider the full set of four-coordinated structures, which have an ideal angle of 109.5°. If all of these were to have formed tetrahedrons with ideal angles, and bond lengths that lie in a small range, then very few sites are required to fully sample this landscape. For this purpose, standard deviation (SD) is a good metric because it precisely encapsulates the idea of how distorted each bond angle and bond length is from a mean. What we want to study is the range of SD distributions across the different sites for a given coordination number to assess how diverse our landscape truly is. Pooled relative standard deviation (PRSD) was used to combine the SD of the bond angles and the SD of the bond lengths into one single metric that describes the site (Figure 9, step 3). Relative here refers to the fact that, because standard deviations of bond angles will be much larger than that of bond lengths, these are "weighted" by dividing each site's bond length SD by the site's mean bond length, and similarly for the bond angles, giving each equal contribution, as shown in equation 3.

$$\widetilde{\sigma_{\text{pooled},\iota}} = \sqrt{\frac{(n_{b,i}-1)\widetilde{\sigma_{a,\iota}^2}+(n_{a,i}-1)\widetilde{\sigma_{\text{b},\iota}^2}}{(n_{b,i}-1)+(n_{a,i}-1)}} \tag{3}$$

Here, $n_{b,i}$ and $n_{a,i}$ refer to the number of bonds and the number of angles, respectively, per site. $\widetilde{\sigma_{b,\iota}}$ and $\widetilde{\sigma_{a,\iota}}$ are the relative bond length SD and the relative bond angle SD, respectively. It is important that the SD computed is within the site and not compared to the mean of an ideal geometry for the coordination number. Although this could work for four-coordinated silicon, with a tetrahedral structure, there is not a single ideal geometry for the five-coordinated sites, much less an ideal angle or bond length. Therefore, a measure of distortion must be an intrinsic comparison to the site itself and the variation within it. In other words, the pooled relative SD values for each site give a measure of how symmetrical the site is, with an ideal tetrahedron receiving a much different score than a trigonal bipyramid, due to the latter having multiple angles and often also bond lengths that describe their ideal geometry. The distribution of these, however, gives a good idea of how many sites need to be sampled. If there is large variation in the bond angles and lengths, then there is a larger range of PRSDs and so more sites are likely to have to be sampled. PRSDs were plotted onto histograms, an example of which can be seen in **Error! Reference source not found.**a, w ith an appropriate number of bins, determined after assessing how distinct the edge bins of the histogram were from each other, as well as neighboring bins.

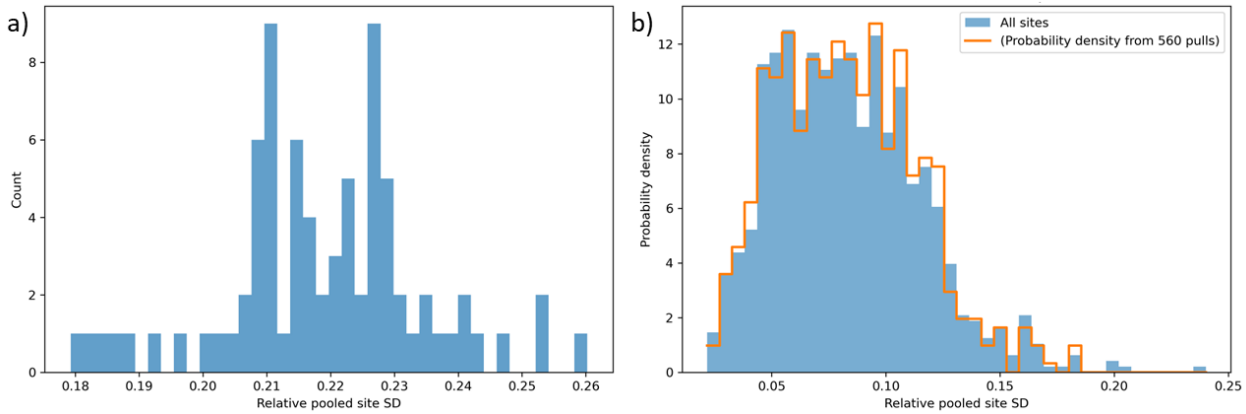

Figure 13. a) PRSD of five-coordinated silicon sites, using 15 bins, and b) PRSD of four-coordinated silicon sites (blue), overlayed with the probability density line histogram (orange) from randomly selecting 560 four-coordinated sites, using 40 bins.

For an appropriate number of sites sampled, it must hold true that if the sites were to be randomly selected, they must follow a similar distribution to that of all sites. The problem of selecting an appropriate number of sites to be sampled then becomes a question of determining the number of random sites that can match the PRSD distribution to a certain extent. A line histogram of the random pulls was overlayed on top of the "all sites" histogram. Because a weighted selection of sites towards the ones that show a certain degree of disorder more frequently is desired, probability density was used as a metric for the vertical axis instead of count. The "matching" of the two distributions (Figure 9, step 4) was then calculated using the vertical overlap of each histogram, which essentially takes the vertical difference between the two probability density distributions (Figure 13b – example distribution). The desired overlap was set to 0.95.

The number of sites to be sampled was then chosen in an iterative process where the first number of sites to reach the desired overlap was recorded (Figure 9, step 5). Because this is a random pull, the number of sites that reaches the overlap changes every time the process is repeated. For this reason, the process was repeated 151 times for each coordination number, determined necessary for a stable value to be reached. The results for the total number of sampled sites per coordination number, per element are displayed in Table 3, concluding the site selection procedure.

Table 3. Number of sampled sites per CN, with number of bins used and the coverage of the sampling with regards to total site per CN, for each element.

Si	CN	**3**	**4**	**5**	**6**
	Bins	4	40	15	4
	Sampled sites	2	560	71	3
	Sample coverage (%)	100.00	63.85	91.03	100.00
N	CN	**2**	**3**	**4**	
	Bins	10	40	20	
	Sampled sites	48	685	119	
	Sample coverage (%)	92.31	62.61	88.81	

The conversion from crystalline phase to amorphous phase of silicon nitride had various effects on both the geometric and electronic structure of the material. Although average bond lengths remained similar to the crystalline structure, bond lengths displayed large variations across the different sites, and similarly for bond angles. In general, however, local geometry was well maintained with no large artifacts introduced in the melt-quench process. The electronic structure of an amorphous silicon nitride model was also probed (Figure 14) and shows a narrowing of the band gap from 4.27 to 2.66 eV, in comparison to the crystalline system. Additionally, there are two states, formerly in the CBM, with primarily Si character and some N character, that are moved to a lower energy, and into the band gap, which likely correspond to the formation of electron traps within the structure.

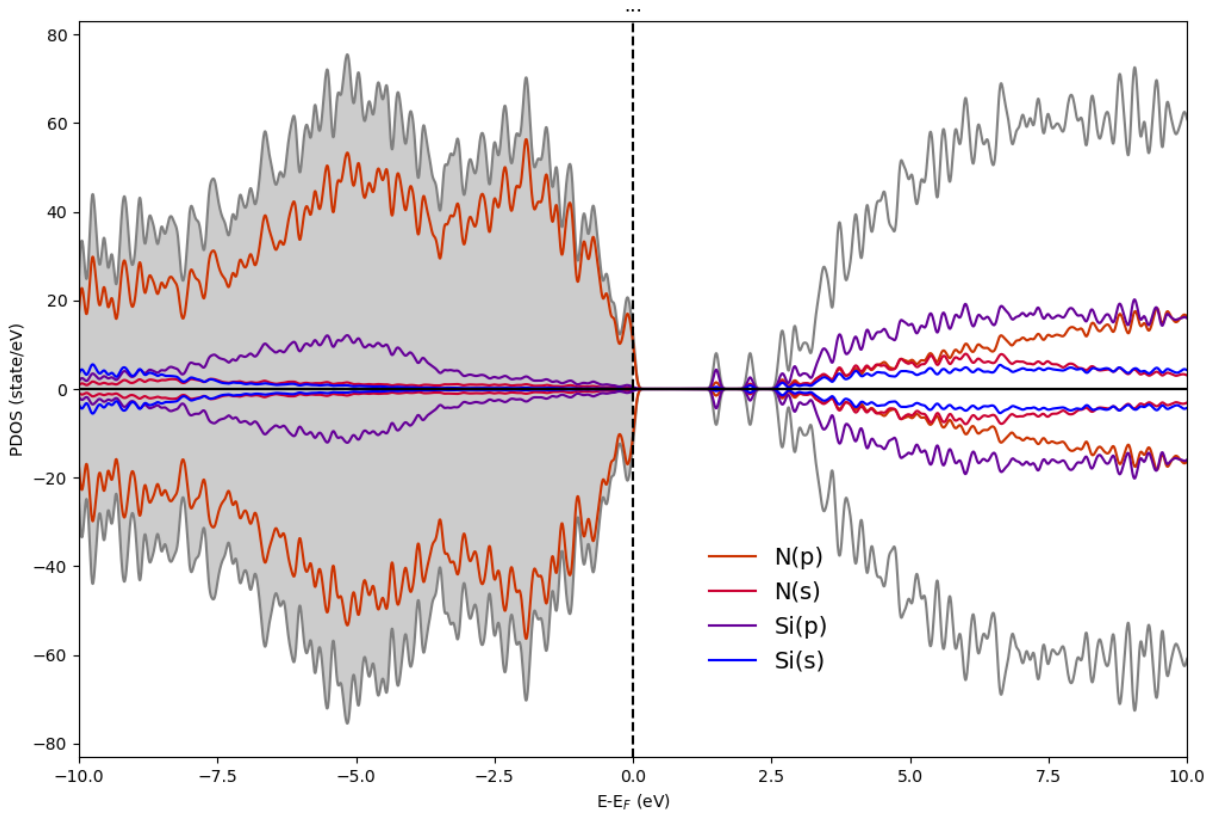

Figure 14. PDoS of the fourth box of the HSE optimized structures, with gray areas showing occupancy.

3.3. Sodium insertion in amorphous silicon nitride

For the insertion of Na, as described in the methods section, (Section 2.2.1), four HSE optimized boxes of amorphous silicon nitride were selected, all containing 280 atoms and each one being representative of a particular electron trap site observed in a-Si_3N_4. Figure 15 showcases the different trap sites and the structural modification of the system upon the trapping of an electron. The first trap site (Figure 15a), pertaining to box one, shows a four-coordinated silicon sharing the extra electron with a neighboring silicon atom forming a Si-Si bond, with one silicon losing a nitrogen atom and becoming three-coordinated. The second electron trap (Figure 15b), pertaining to box 2, shows a smaller geometric distortion than the first, with the elongation of two N bonds, and a shrinking of the angle formed between Si and the other two N atoms. The third trap (Figure 15c), pertaining to box three, displays a lengthening of one of the Si-N bonds. Here, the electrons in the now broken N-Si bond remain on the nitrogen as an anion, and the extra electron rests on the now three-coordinated silicon. Finally, the last electron trap, pertaining to box four, involves a three-coordinated trigonal planar Si that, upon receiving the extra electron, moves out of the coordination plane, elongating the Si-N bonds.

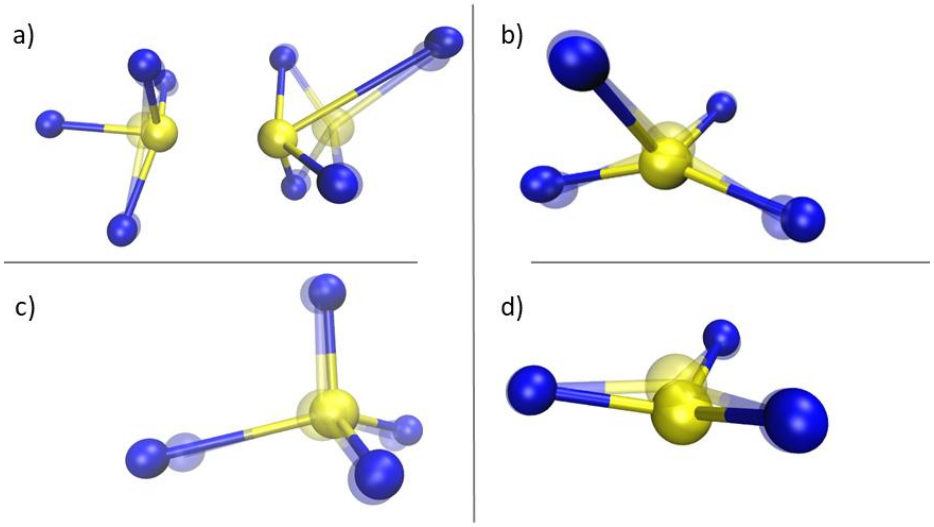

*Figure 15. Electron trap sites before (faded color) and after and after trapping an electron (bold color) of **a)** box 1, **b)** box 2, **c)** box 3, and **d)** box 4.*

In order to insert Na atoms into these four boxes, we employed our above developed sampling method to conduct a coordination number analysis, using the same distance cutoff of 2.25 Å found in the development of the sampling scheme. This was done in order to tally up the number of sites per coordination number for each of the boxes, as was previously executed. Now that we know precisely how many sites there are per coordination number for each element, we can employ the results of the sampling scheme to select which sites will be sampled. Based on the percentage of sites that need be covered per coordination number (Table 3), sites were randomly selected for sampling until the required number of sites was reached. A total of 186, 188, 189, and 185 sites for boxes one through four, respectively, were selected for sampling.

At this point, the specific sites to be sampled have been selected. However, the space around these sample sites, as was seen before, is not symmetrical in terms of chemical environment that they would be subject to. This means that we must know decide where, in the space around each selected site, to place the Na atom. For this, a Voronoi tessellation of the space centered around each atom was conducted. This involves, as the name suggests, tessellating the structure by placing planes at the midpoints of lines connecting the center atom to its neighbours.[73] The planes then become the faces of the Voronoi polyhedron, and where two planes intersect become the edges of the polyhedron. The tessellation is constructed in such a way that guarantees the Voronoi volume contains all points that are closest to the center of the polyhedron than to any other center.[73] For this work, only the largest face, representing the largest empty space, is considered in order to minimize electrostatic repulsions with neighboring atoms. Following this method, we first place the sodium on the line to the center of the largest face at a distance of 2.0 Å from the center atom and is then moved, at a fixed distance from the center, to the location that minimizes the distance to other atoms, with a minimum cutoff of 1.7 Å (Figure 16). This cutoff was set to be approximately 1.5 times greater than the covalent radius of sodium. No sites were discarded based on this cutoff. Voronoi tessellation took place using the *freud* software package (v.1.2.1)[74].

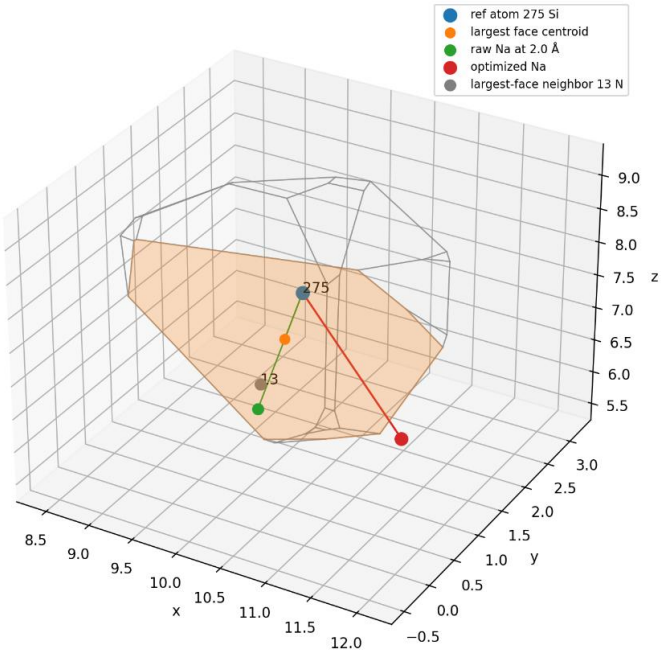

Figure 16. Example Voronoi tessellation of a silicon atom (blue) for sodium insertion. The largest face (orange) and the nitrogen atom (gray) pertaining to it. The optimized sodium (red) comes from minimizing the interaction with neighboring atoms after initial placement (green).

3.4 Sodium incorporation into silicon nitride

To assess the energetic stability of sodium storage in amorphous silicon nitride, we next model the sodium incorporation. Firstly, sodium energetics were calculated and separated, per simulation box, based on whether the initial sampling site was silicon-based or nitrogen-based (Figure 17). It was also found that sodium binding energies were equally represented by the initial sampling sites. That is, the sampling scheme used was not shown to bias the binding energies towards the starting geometries, and each sodium atom was able to migrate to a site with lower potential energy, irrespective of where they were initially placed. This is not to say, however, that initial placements have absolutely no impact on final ones. In addition, because such mobility of the atoms within the structure is possible, it is important to assess, of the various sodium insertions, whether any, and which ones, found the same local minima, meaning that these would be duplicate sites, artificially skewing binding energies towards the energy of those sites. It was found, however, that within a distance cutoff of 0.05 Å, there were only two sites per box (approximately 1%) that shared similar coordinates and there were no duplicate formation energies found. That is, formation energies were, in fact, varied and dependent on their position within the structure. How exactly the location of these atoms within the structure determines their binding energies requires an analysis of the coordination environment of each atom, and a characterization of common structural features of the relaxed sites.

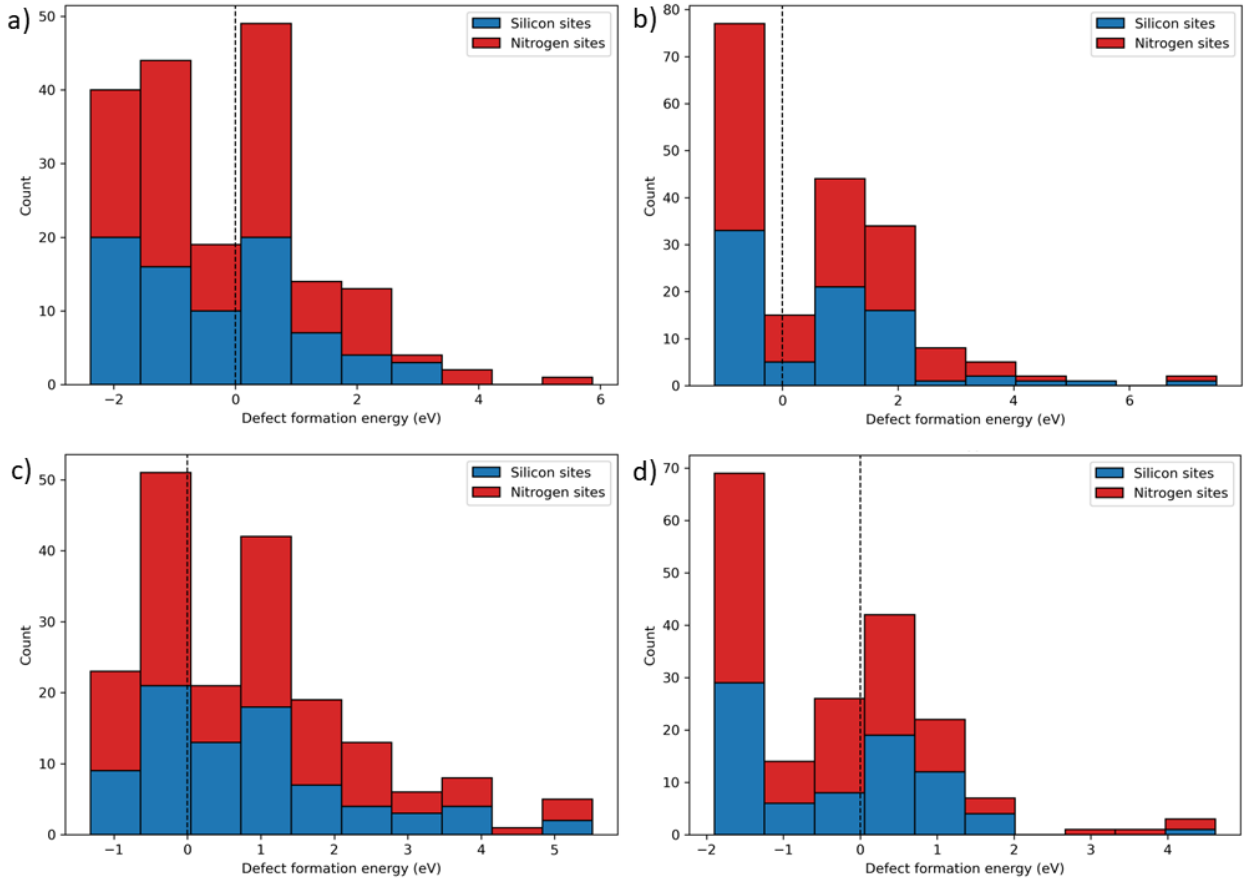

*Figure 17. Calculated defect formation energies stacked histogram, split into Na binding sites inserted next to silicon atoms (blue) and Na sites inserted next to nitrogen atoms (red), with a dashed line at the 0 eV mark, for **a)** box one, **b)** box two, **c)** box three, and **d)** box for.*

To understand the coordination environment of the incorporated sodium atoms, a coordination shell that includes first-neighbor atoms must be constructed. To ascertain what the radius of this shell should be, or in other words, what range of distances will be included in the search for neighboring atoms, the pair distribution function (equation 2) was employed, with data pooled from all four boxes (Figure 18). Here, Na-N and Na-Si distances were treated separately, avoiding the assumption that silicon and nitrogen would have equivalent interactions with sodium, and allowing for two separate cutoffs to be set for each element, if required. Unlike the Si-N pair distribution function (Figure 10), however, no clear-cut coordination shell was found. Although it is clear that silicon and nitrogen require separate cutoffs from the location of their PDF peaks, there is a great deal of overlap between the two, likely involving a mix of first-neighbor and second-neighbor atoms. This is likely indicative that the coordination environment for the Na incorporation sites is varied, including a wide range of interaction distances. This means that, unlike before, a single coordination number, to define each site, found by virtue of counting the number of atoms in the coordination shell, is not a suitable metric for this analysis. A less nuanced, more general approach to the problem is required.

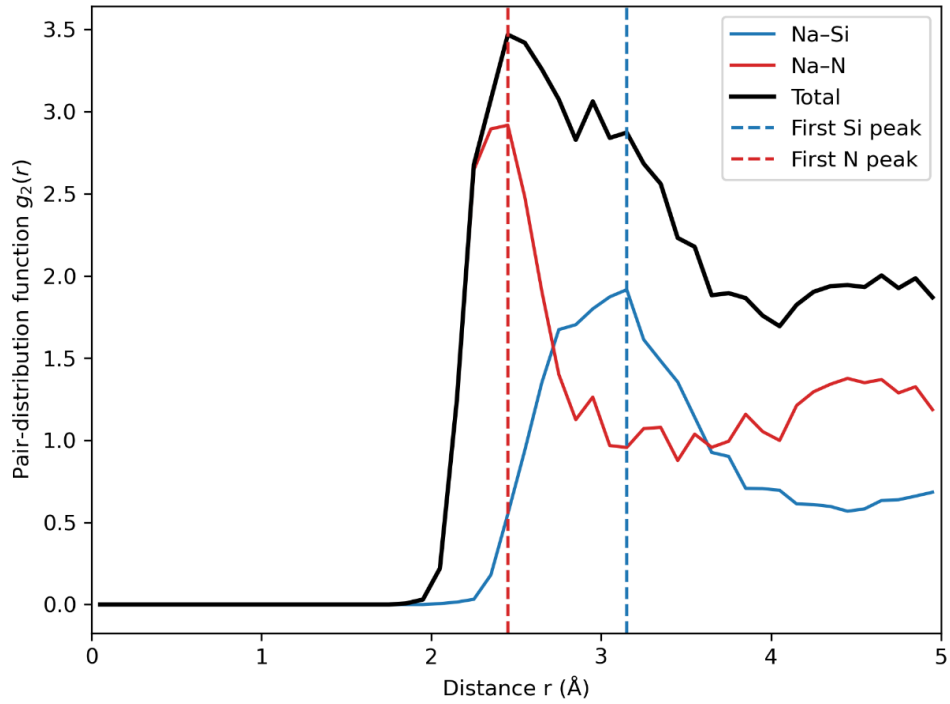

Figure 18. Pair distribution function of total Na interactions (black) subdivided into Na-N (red) and Na-Si (blue) interactions, alongside their respective first peaks (dashed lines).

At this point, we wish to investigate the local environment around Na, and which sites it preferentially binds to. However, without having precise information on what the first coordination shell of each sodium atom is, the distance cutoffs were estimated based on what was found from Figure 18, and the impact that this has on the following results is further discussed in Section 4. Here, larger cutoffs than those used for Si-N, were employed, set at 2.5 Å for nitrogen and 3.0 Å for silicon. The approach used to determine which sites Na preferentially binds to was to first identify what the closest atom to each sodium was. It was found that

nitrogen was the closest atom to sodium in over 94.1% of sodium insertions, and since most silicon atoms were substantially farther away (Figure 18), this indicated that sodium seemed to prefer coordinating with nitrogen over silicon. Furthermore, the spin moments of all incorporated sodium atoms were analyzed, and it found that in all cases, Na lost an electron to enter its more stable cationic state, which would make electrostatic interactions more favorable with a negatively charged nitrogen, than a positively charged silicon. This finding guided further analysis to focus on how the number of coordinated nitrogen atoms impacted sodium binding energies and whether the presence of silicon had an influence on these. Subsequently, all sites, across all boxes, were categorized by the number of N atoms present in the cutoff sphere, as well as whether silicon was present in the coordination or not and what its mean distance to Na was (Figure 19).

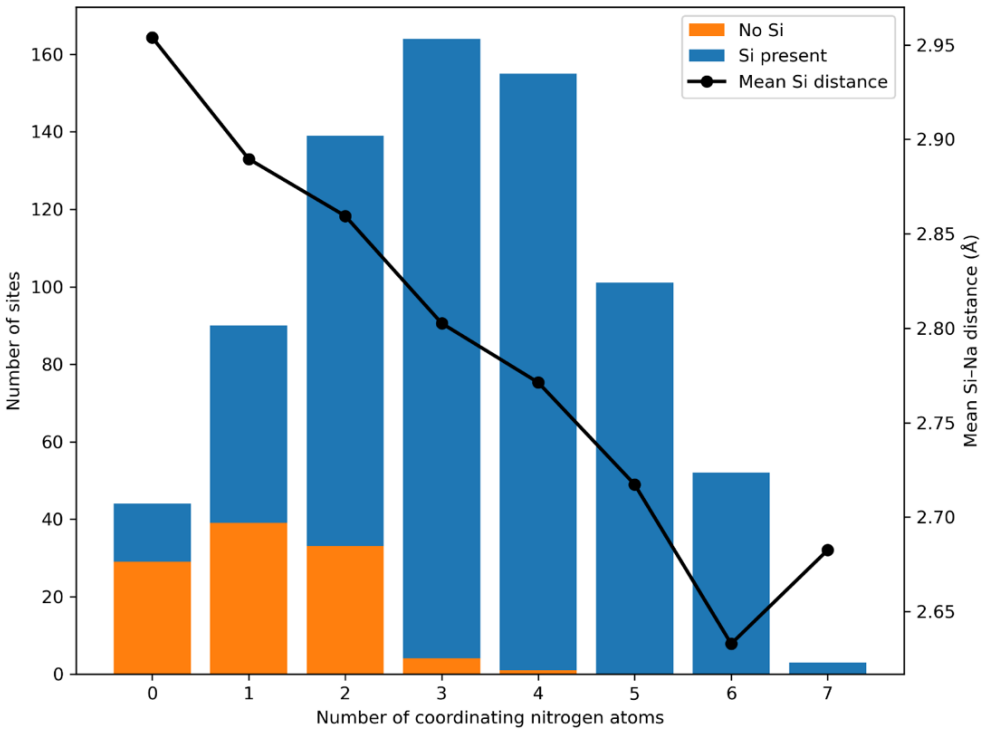

Figure 19. Sodium coordination environment stacked histogram binned by number of nitrogen in the coordination sphere, with the bottom stack (orange) representing the Si absent sites, and a line graph (black) representing the mean Si-N distance.

Sodium atoms were found to coordinate two, three, and four nitrogen atoms the most, representing 61.2% of sites. Furthermore, the distribution resembles a bell curve with a central distribution around three-coordinated nitrogen. This could imply the formation of NaN_3, similar to what was seen for lithiation of a-Si_3N_4, where LiN_3 was also a commonly formed structural motif.[4] There are also a few instances where silicon is present, but nitrogen is absent (Figure 20a). Given, however, a large enough space in the structure, it is possible for silicon to be the only atom within a 3 Å distance to sodium, as is seen by the mean Si bond length surpassing 2.95 Å (Figure 19). The presence of such larger spaces within the structure is directly evidenced with instances where neither nitrogen nor silicon are present in the coordination of the sodium atom, within the cutoff distance. Figure 20 also shows that as the number of nitrogen atoms coordinated to Na increases, the mean Si distance to Na decreases. The fact that silicon presence increases with increasing

nitrogen coordination likely indicates that many of the present silicon atoms are second-neighbors to the sodium, as is seen in Figure 20b, Figure 20c and Figure 20d. This further supports the idea that what is seen as increasing nitrogen coordination is most likely a decrease in void size.

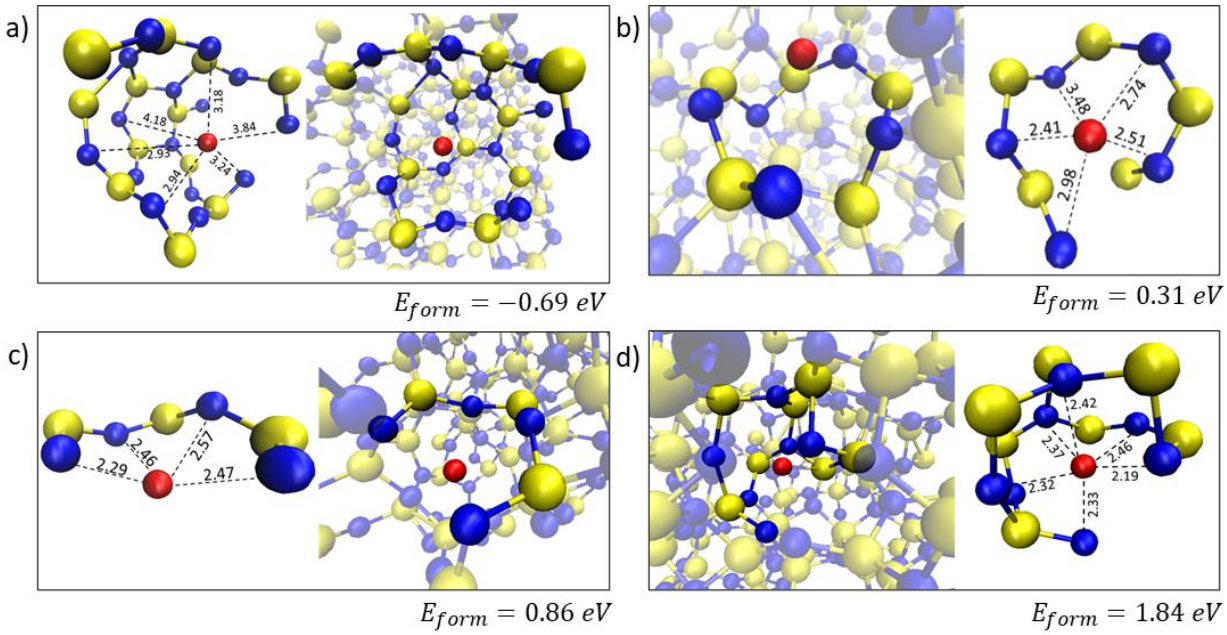

Figure 20. Na insertion sites with nearby atoms (Si in yellow, N in blue) depicted, with corresponding binding energies for each site, and distances to nitrogen atoms displayed in Å, of Na (red) ***a)*** *with no nitrogen atoms within the cutoff,* ***b)*** *a single nitrogen atom present within the cutoff* ***c)*** *three nitrogen atoms present within the cutoff, and* ***d)*** *six nitrogen present within the cutoff.*

The average sodium binding energy, across all boxes, was found to be 0.398 eV, which is far lower than what was found in the crystalline system, in accordance with our hypothesis and suggestions in the previous literature.[16,32,34,41] The range of sodium binding energies, from -2.383 eV to 7.510 eV, however, is far wider than what was obtained for the crystalline system. Furthermore, there was a distinguishable difference in average binding energies between the four boxes, standing at -0.176, 0.702, 0.830, and 0.236, for boxes 1, 2, 3 and 4, respectively, though this is largely attributed to the different electron trap sites present in the system. To gain insight into the available Na storage sites, and which sites are energetically favored, average formation energies for each of the categories of environments presented in Figure 19 were calculated, considering instances when silicon is present in the coordination sphere and when it is not, separately (Figure 21). There is a clear trend formed with weaker binding energies as the number of nitrogen atoms in the coordination sphere increases. For Na with up to three coordinated nitrogen, the average defect formation energies are negative, meaning energetically favorable Na incorporation into the structure. For Na sites with beyond four coordinated nitrogen atoms, there is a sharp weakening of the formation energies, which suggests energetically non-favorable Na incorporation. Nonetheless, as the number of nitrogen in the Na coordination shell increases, there is a larger range of binding energies. This indicates a large variety of sampled Na storage sites, showing that the selected categories on which this analysis was based on were quite general. The results are as expected from what could be inferred from Figure 19, where it is likely

that, as nitrogen number increases, there is increased steric repulsion, as the sodium atom is forced into a smaller space. This can also be seen in Figure 20, where, the lowest energy sites are the ones where Na distances to other atoms are maximized.

The lithiation of a-Si_3N_4 also showed a similar trend, where lithium atoms with coordination numbers above three, had, in general, higher defect formation energies.[4] There is also a trend seen in the system where the presence of silicon in the coordination sphere weakens the binding energy, although for more than two coordinated nitrogen, this pattern cannot be established, as there are only a few sites where Si was not present (Figure 19). The decrease, nonetheless, could signify that the positively charged silicon has a repulsive electrostatic interaction with sodium, weakening the binding energies. In general, however, it was seen that steric effects govern Na binding energies, and the number of available sites that reduce this steric hinderance for sodium needs to be further investigated in order to assess the viability of a-Si_3N_4 as an anode material for NIBs.

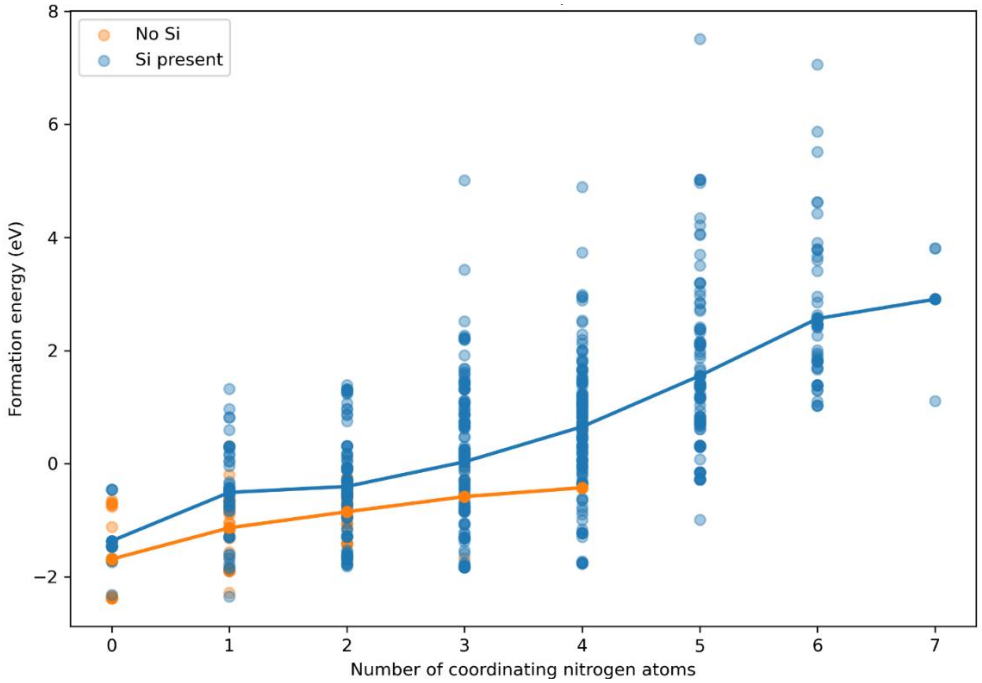

Figure 21. Defect formation energies for each number of coordinated nitrogen atoms, with (blue) and without (orange) presence of Si atoms in the coordination sphere.

Up until this point, we have focused on the geometric description of the different Na storage sites. Next, we calculate the electronic structure of the various environments of each of the site categories described above, representative sodium insertions were selected of the same categories as the ones presented in Figure 20, and their PDoS calculated (Figure 22). Because it is expected that the specific trap sites of each box have an impact on the electronic structure, sites were selected originating from the same box (box four), allowing for a level comparison. In all cases, the state at the Fermi line, is a silicon site, showing no Na character, and is where a deep intrinsic electron trap forms, approximately 2 eV from the CBM, meaning that it takes a lot of energy to remove the electron from this site. This can be seen coming from the non-

sodiated structure (Figure 14), where once an electron is added, the occupied state moves from the CBM into the band gap. This is seen across all four sites and shows that it is largely independent of Na site.

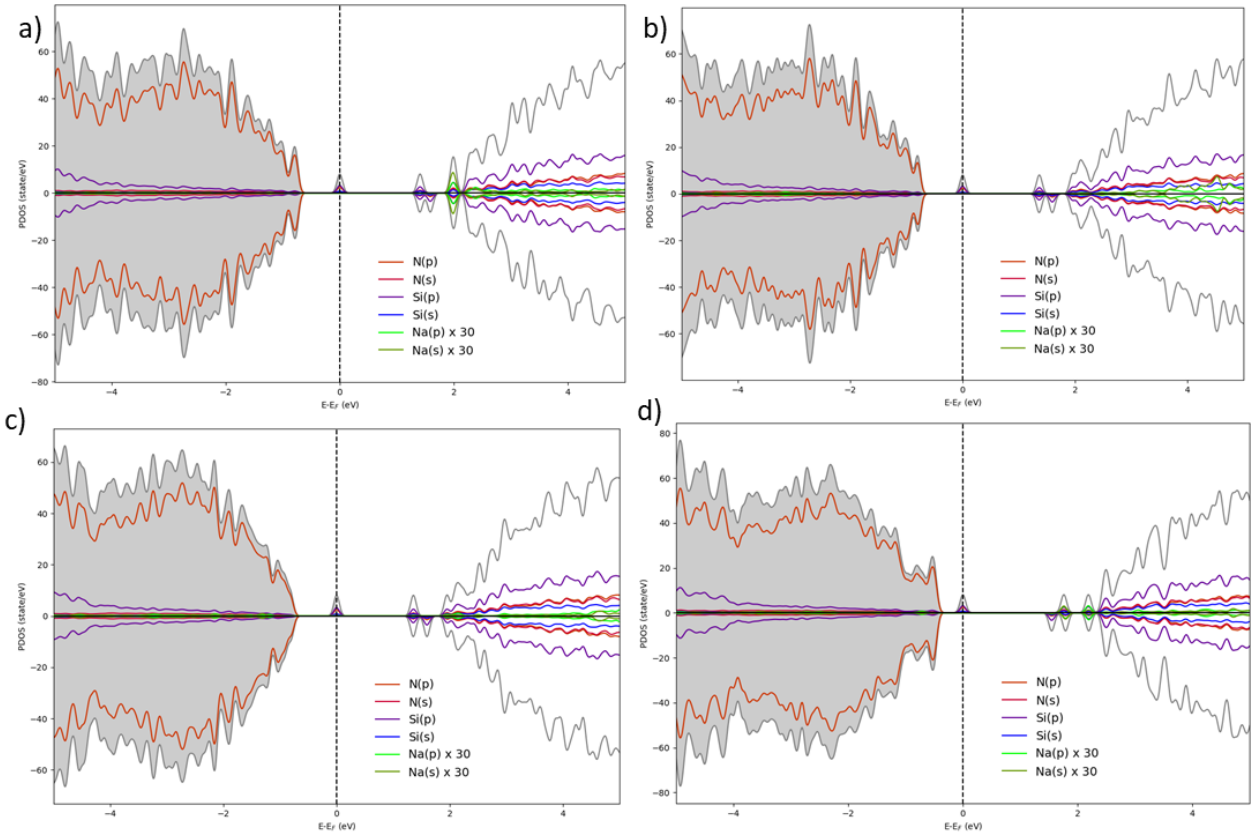

Figure 22. PDoS with sodium, and gray shaded areas demonstrating occupation, of box four with sodium insertion categories: ***a)*** *N=0 with no Si present,* ***b)*** *N=0 with Si present,* ***c)*** *N=3 with Si present, and* ***d)*** *N=6 with Si present.*

Examining the PDOSs for the N=0 states without Si (Figure 22a) and with Si (Figure 22b), there is a stark difference in their electronic structures, where unoccupied Na states near the CBM show for site lacking Si. The fact these are unoccupied shows that sodium is in its cationic state, and it is unlikely there would be no charge transfer to a nearby atom. In addition to this, the fact that the states are close to the CBM, indicates that sodium is interacting with the trap site, or is inducing a new trap site, which could not be seen from the analysis presented in Figure Figure 19 and Figure 21. The difference between the plots in Figure 22a and Figure 22b was not expected as, aside from the Si present in one, at a distance of 2.99 Å, both sites lacked N in their coordination shell, and the difference in binding energies between the two was less than 0.003 eV. That is, it was expected that these two would share similar electronic structures as they are both fairly distant from other atoms and incorporated equally favorably into the structure. Nonetheless, both the cutoff utilized for nitrogen and the effect that sodium has with electron traps could explain why there is an interaction difference between the two Na sites, warranting further investigation. Now comparing the three-nitrogen coordination (Figure 22c) to the six-nitrogen coordination (Figure 22d), there are differences observed between the two, where the latter presents sodium states close the CBM, pushed to a lower energy.

Considering that sodium atoms with six-coordinated nitrogen are surrounded by a larger number of close atoms, the triggers for the occurrence of lower energy Na states could involve larger electrostatic repulsion, as evidenced by the large defect formation energies, or more pronounced structural modification, or even interactions with trap sites. However, with the data in hand, we cannot differentiate between these.

4. DISCUSSION

Sodium's incorporation into silicon nitride was demonstrated to be highly varied in terms of stable Na storage sites. In crystalline silicon nitride, β-Si_3N_4, the process of sodium insertion was energetically unfavorable, with incorporation energies ranging from 2.34 eV to 7.69 eV. Structural changes were governed largely by steric repulsion, mostly seen in the narrow channels, where the short interatomic distances increased the potential energy of the system, leading to high formation energies. Even in the large channels, though minimal structural changes were seen, sodium incorporation was far from favorable. These findings are expected and in line with the bad anode performance of the crystalline structure seen by Martín-Gil *et al.* (2003)[32]. As crystalline silicon nitride was not found be stable, we turn to amorphous silicon nitride, a conversion-type anode, which have been shown to display larger capacities than intercalating-type anodes.[4–6]

In general, the amorphous models had a large range of structural motifs and varied chemical environments for potential sodium storage sites. In this thesis, the over-coordination effect of the classical potentials used, generated more five-coordinated silicon atoms and four-coordinated nitrogen atoms than are physically representative of the amorphous structure.[35] Despite this, 91.0% and 88.8% of those sites were sampled, respectively, and the effect that the over-coordination had on the localization of sodium in the structure is likely minimal as it was seen that these were able to dislodge quite readily from their initial placements, to find nearby potential energy minima. An interesting question to ask, however, is how the coordination of Si and N impacts the available binding sites for sodium. This question, in essence, asks how changes in the silicon nitride network geometrically impact available Na storage environments. As the number of studies assessing anode materials using atomic-scale computational methods increases[6], making comparisons across these studies, with the various generation methods available, all capable of dramatically changing the geometric motifs of the material, necessitate an understanding of how the degree of amorphousness impacts metal incorporation into host structures. Furthermore, more research must be done on the effect that sub-stoichiometry has on sodium binding energies, as it also has a large impact on the amorphous structure, and could help explain the large range of capacities seen across different ratios.[28,39,40]

In general, sodium binding energies were far stronger in the amorphous structures than in the crystalline one, with 48.8% of Na storage sites showing a negative formation energy, indicating favorable incorporation into the host structure. The suitability of a-Si_3N_4 as an anode material for NIBs is intrinsically linked to how favorable sodium's insertion into the structure is, which was demonstrated to be highly dependent on how it interacted with the structure. In the amorphous system studied in this investigation, sodium displayed a clear interaction preference for nitrogen over silicon, where in over 94% of cases, N was the closest atom to Na. This is not to say, however, that all nitrogen interactions were favorable for Na. In general, there was a clear trend that showed increased incorporation energies as the number of nitrogen atoms in the coordination shell increased (Figure 21). Defect formation energies for Na sites with more than

three coordinated nitrogen atoms had, on average, unfavorable incorporation into the structure. It was also seen that the frequency of sites with over three coordinated N decreases as a function of the number of N. That is, beyond three-coordinated N, Na sites decreased in number as the CN increased, suggesting a strong inverse relationship between incorporation energy and frequency of site population. As the number of N in Na's coordination shell increased, the mean silicon distance decreased (Figure 19), reducing the amount of space around the Na atom, which is in line with what was seen for some of the inspected sites (Figure 20). This increase in electrostatic repulsion between Na and the surrounding Si is likely what drives the weaker binding energies. Despite this, lower coordination numbers, however, having stronger binding energies, sites occurred less frequently than the three-coordinated ones, likely as a result of the a-Si_3N_4 structure in which it is placed in, where sites in which sodium could have rested that minimized its steric hinderance were less common than those where some level of electrostatic repulsion is present, weakening Na's binding energy. With increasing attention being brough to understanding the structural evolution of amorphous structures during fabrication, if possible, the synthesis of larger voids, likely through faster cooling, would likely favor the incorporation of sodium into amorphous silicon nitride, and increase its capacity as an anode material.[75]

In this study, Na-N, and Na-Si interactions were important in determining how sodium is incorporated into the amorphous structure. N-Si interactions were equally as important, determining the structural motifs present in the amorphous constructions. Distance cutoffs were set to determine a coordination sphere, inside which all atoms were considered to be interacting. In general, this worked well for the development of the site sampling scheme, where a clear first and second coordination shell were visible (Figure 10). However, when it came to establishing patterns in the assimilation of sodium into the amorphous structure, the interactions were much more varied, at a large range of distances, making it difficult to distinguish between first and second neighboring atoms (Figure 18). The impact this may have had on results is varied. The pattern of weaker binding energies with increased nitrogen coordination is likely not affected. However, the true coordination number may have been higher. Firstly, it was seen by means of visual inspection, that many sites included nitrogen atoms at a distance of 0.1 to 0.3 Å above the cutoff of 2.5 Å, which were also likely influenced by sodium's presence in the structure. Similarly, for silicon, some sites displayed silicon sites that were also just outside the cutoff distance of 3 Å, though here it is difficult to say how likely these were to have been interacting. Nonetheless, the fact that some Na atoms were found to be completely uncoordinated is a strong signal that the distance cutoff for both Na-N and Na-Si were likely underset. This is because, since no instances of neutral Na were found, all sites involved Na as a cation, forcing a Coulombic interaction to occur, which cannot be analyzed without appropriate distance cutoffs. It is clear that a more nuanced method to sample the sodium sites and determining coordination would be required. Taking electron sharing into account could be of great use in creating such a method for covalently bonded structures. However, for ionic interactions, as is usually the case with sodium, more care needs to be taken in selecting distance cutoffs for coordination shells, potentially on a site-by-site basis, where individual lengths are probed and a complex network of second-neighbor distances could be established. Nonetheless, this lies outside the scope of this thesis and requires further investigation.

Because sodium incorporation into the network is governed by electrochemical interactions with the structure, it is useful to compare the incorporation of sodium into a-Si_3N_4 to the incorporation of electrochemically similar elements into the same structure. The lithiation of silicon nitride also showed a similar trend of increasing incorporation energy with increasing nitrogen coordination of the sodium atom.[4] However, for lithium sites, coordination numbers smaller than or equal to three were far more common than

those above three, which can likely be attributed to sodium's larger size. For lithium, the matrix formation process in the conversion reaction of silicon nitride was demonstrated to be governed by bipolaron formation, linking silicon atoms together, and forming the experimentally seen Si-rich region.[4] There, lithium was involved in the charge trapping process, be it via interactions with intrinsic trap sites, or the formation of induced trap sites. Many of these involved lithium interacting with silicon atoms. Figure 22a and b show sodium states lower in energy, and shifted into the band gap, close to the CBM, likely suggesting sodium's interaction with the structure's trap site or the formation of a new one. However, we cannot speculate as to the way in which sodium is involved in the charge trapping process and as such we cannot conclude that a conversion reaction of silicon nitride with sodium would form a matrix in the same manner as lithium. Therefore, future studies should focus on understanding the interactions or effects that sodium has with or on the trap sites of a-Si_3N_4, Furthermore, though many of the induced trap sites in the lithiation of a-Si_3N_4 involved Li atoms that were coordinated by two and four N atoms, which were frequently seen for sodium, it is nonetheless possible that Na's larger size could prevent it from accommodating a Si atom to the point of forming a strong interaction, without severely affecting its coordination with nitrogen atoms. Additionally, the number of sodium atoms inserted at a time, one, gives insights into how each insertion site may behave, and an idea of how sodium interacts with the different motifs of the amorphous structure. But as was seen with the crystalline system, there can be a great deal of interplay between multiple sodium atoms and the structure. In the amorphous system, multiple sodium insertions would be required to see bipolaronic formations, as were seen with lithium atoms. To gain a better understanding of the manner in which sodium interacts with the Si trap sites, and the effect this has on the structure, requires further investigation.

5. CONCLUSION

In this investigation, we presented a DFT study on the incorporation of sodium into amorphous silicon nitride to assess its storage properties as a conversion-type anode for NIBs. Sodium insertion into silicon nitride resulted in a large range of coordination environments and binding energies. β-Si_3N_4 was confirmed to be energetically unfavorable as an anode material for NIBs, with incorporation energies ranging from 2.34 eV to 7.69 eV. In the amorphous structure, sodium was found to interact preferentially with nitrogen. Binding energies for Na storage sites, ranging from -2.383 eV to 7.510 eV, were found to be highly dependent on Na site environment, with increasing N coordination showing weakened binding energies. The Na storage sites displaying the strongest binding energies showed low Si character and between one and three coordinating nitrogen atoms, as was also seen in the electrochemically similar lithiation of a-Si_3N_4. With 48.8 % of Na storage sites showing favorable energetic incorporation, a-Si_3N_4 shows promise as an anode material for NIBs. Nonetheless, questions remain as pertaining to sodium's interaction with electron traps in amorphous silicon nitride, meaning that more investigation is needed, requiring multiple, consecutive sodium insertions, and a more nuanced approach to identifying sodium interactions and their coordination environment. These are key to understanding the matrix formation process in the conversion reaction of amorphous silicon nitride, and thus, addressing the feasibility of amorphous silicon nitride as an anode material for NIBs.

CRITICAL REFLECTION

Writing a bachelor's thesis was quite a bit more difficult than I imagined it to be. Of course, this might be the most obvious statement I could make and I imagine many of my peers have written something similar. In many ways, however, this thesis eased my mind about what kind of expectations are set in academia and has made me far more excited about delving further into it. I would like to share a conversation I overheard in the office space at the ARCNL institute, where I conducted my thesis. It involved a PhD candidate with a physics background, asking a post-doctoral researcher in the group a question regarding the structure of benzene. The post-doctoral researcher answered them with another question: “Are you familiar with the pi orbitals around aromatic rings?”. They weren’t. I couldn’t believe it! This was taught to me during the first year of my undergraduate course and a PhD candidate, having many years of research experience more than me, didn’t know. Then, however, is when it occurred to me that getting titles and building years of research experience are not about gaining as much knowledge as possible, but about learning how to learn. In many ways this ties in directly to my thesis. The field pertaining to this thesis was not one that I had heard of in lectures or had seen in practical classes. It required serious dedication to self-learning and a passion to understand the literature and be able to explain what I researched. Reflecting on how I approached problems in science when I first started my undergraduate degree, and what I was able to achieve with this thesis made me realize just how much progress I have made.

Throughout the process of writing this thesis, however, a few things I could have done better came to mind. Firstly, writing as you go is one of the most important things that I should have kept more in mind. What I mean by this is not writing sections of the thesis beforehand so that it doesn’t all come at once, but instead reflecting on things as you have just done them. For example, when conducting the exhaustive sampling scheme for this thesis, which involved many steps, a better system for keeping track of what the previous step was, what next step should be, and why I am taking this particular route would have helped. This last part, especially, is the easiest to forget months after the fact and justifying why a certain course of action was taken is one of the many pillars of science. This is not to say that I did not keep track of these things, but at certain times I found myself wishing that I had written a particular detail down that was now too late to remember. Secondly, though I always thought of myself as being good at time management, this thesis taught me otherwise. In hindsight, I should have planned more time to analyze my data. Although I do believe there needs to be a balance between the time spent writing and analyzing, after all, a good analysis still needs to be well explained. I believe that given a few more days of work, however, I could have delved deeper and understand what the charge trapping process for the sodium’s in the system was. Though I do believe that I was able to come to meaningful conclusions, it was frustrating to write the last parts of the results section, knowing that given more time, I could have told a more complete story.

Having had the opportunity to be a part of the ARCNL institute gave me a glimpse of what a career in the sciences looks like, and I am incredibly grateful to my supervisor for having granted me this opportunity. It gave me peace of mind to see how devoted and interested everyone was in their work, and I regained some faith that there are people out there who don’t have agendas, but a true, deep passion for science.

APPENDIX 1 – CONVERGENCE TESTING

Convergence testing was conducted on basis sets, supercell size, cutoff energy, and relative cutoff energy. Base computational parameters were set at a cutoff of 650 Ry and a relative cutoff of 70 Ry, on a 3x3x3 β-Si_3N_4 supercell, based on Cottom et al. (2025)[4], and adjusted as convergence testing took place.

Basis set selection

The basis set in a DFT calculation is a collection of functions that determines how the valence electrons of each atom in a system are mathematically described.[46] The zeta of a basis set gives how many functions are used to describe each orbital. That is, from single zeta to quadruple zeta, one can dramatically increase the calculation's accuracy by using one to four functions per orbital, respectively, but also dramatically increase the computational cost of the calculation.[46] Convergence testing of several basis sets available for the CP2K software and the desired elements (Na, Si, N), was conducted, namely one single-zeta (SZV-MOLOPT-GTH)[76], three double-zeta (DZVP-MOLOPT-SR-GTH, DZVP-MOLOPT-PBE-GTH, and DZVP-GTH-PBE)[76], and one triple-zeta (TZVP-MOLOPT-PBE-GTH)[76] basis sets. The single zeta basis was found to take the longest to converge at 5280 seconds at 64 cores, likely not being complex enough to allow the functions to fully describe the system, and so was disregarded from the results shown in Figure A1. The basis sets pertaining to the MOLOPT family all converged within a narrow, and lower, energy range. From these, the short range (SR), DZVP-MOLOPT-SR-GTH basis set converged in the shortest amount of time, and so was selected to be used in this investigation.

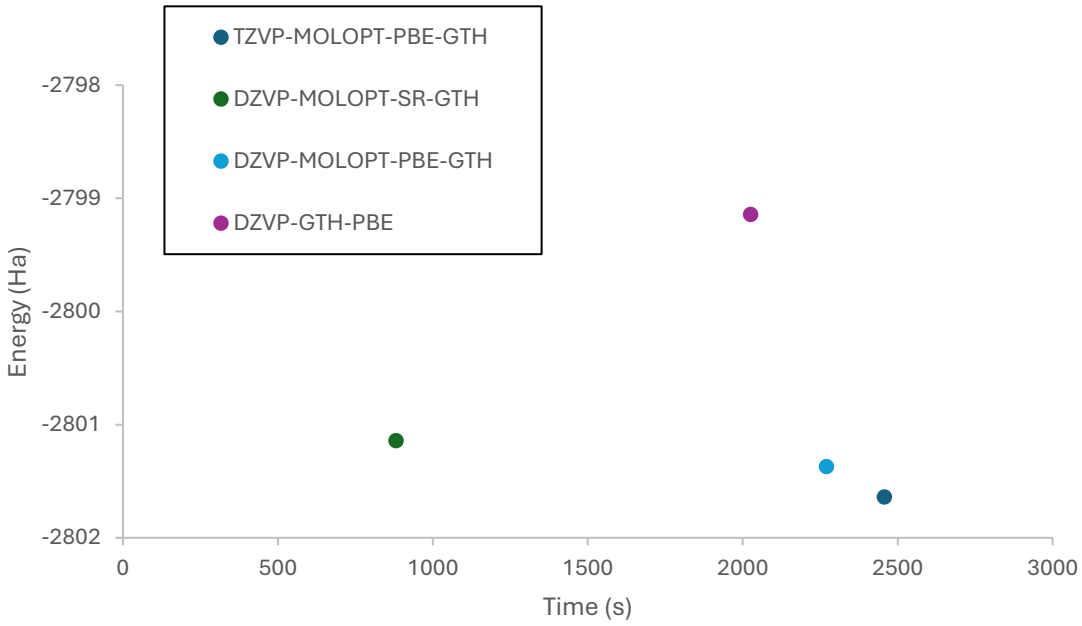

Figure A1. Scatter plot depicting energy versus time taken to converge for the tested basis sets.

Establishing supercell size

CP2K uses atom-localized Gaussian orbitals to describe its system, making calculations much less sensitive to k-point sampling, as the wavefunction changes less drastically over the Brillouin zone, over which most properties of interest are integrated over.[77] Nonetheless, k-point sampling is still a pivotal part of any calculation and CP2K often defaults to a single Gamma (center) point. Because of the inverse relationship between reciprocal space and real space, the larger the size of the cell used, the more representative the sampling of a single point in the Brillouin zone is. For this, convergence testing was conducted for the crystalline system, with a NxNxN supercell, with N = 1, 2, 3, and 4 (Figure A2). For comparison, literature values of the lattice constants from computational studies were taken into consideration. The supercell with N=1 showed the worst agreement with literature data, with a lattice vector A 6.20 Å long, and was not included in figure X. Both the supercells with N=3 and N=4 showed great agreement with other computational studies. Since N=3 used significantly fewer computational resources, it was chosen for further use in this investigation.

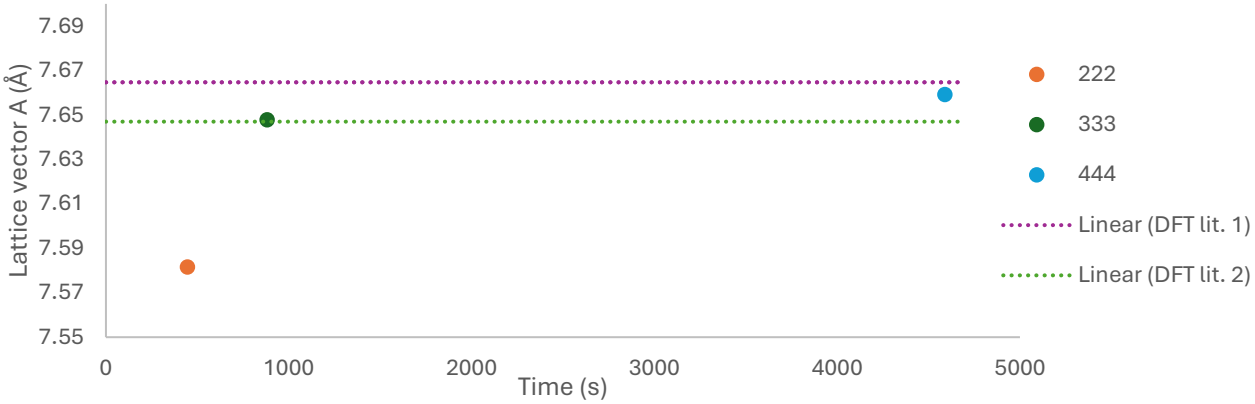

Figure A2. Scatter plot depicting the final lattice vector A, and how long the cell optimization procedure took for each supercell size used. Literature values are also shown, labeled "Linear DFT lit. 1"[78], and "Linear DFT lit. 2"[79].

Cutoff and relative cutoff determination

In CP2K, there is a multigrid system that defaults to four grids. Numerical integration occurs over these grids, where what determines on which grid the integration occurs is the resolution that the function being integrated requires.[80] The finest, highest resolution grid is given an energy value set by what is known as a cutoff energy. As previously discussed, the basis sets used are atom-centered gaussian functions, where these can be tight (covering less than 0.2 Å, for example), or diffuse (potentially covering several Angstrom). CP2K map each gaussian onto a grid such that each gaussian covers roughly the same number of grid points, regardless of how tight or diffuse it is.[80] This mapping is controlled by the relative cutoff energy. However, the higher the number of functions that are processed on the finest grid, the more computationally expensive the calculation becomes. Here, cutoff (figure X) and relative cutoff (figure X) energies were tested for convergence. A relative cutoff of 70 Ry was found to approximately equally distribute functions across the four grids, whilst also being the first to produce the plateaued stable energy, and was therefore used for the remainder of the investigation. With similar reasoning, 600 Ry was found to be the first appropriate cutoff and was also used for this investigation.

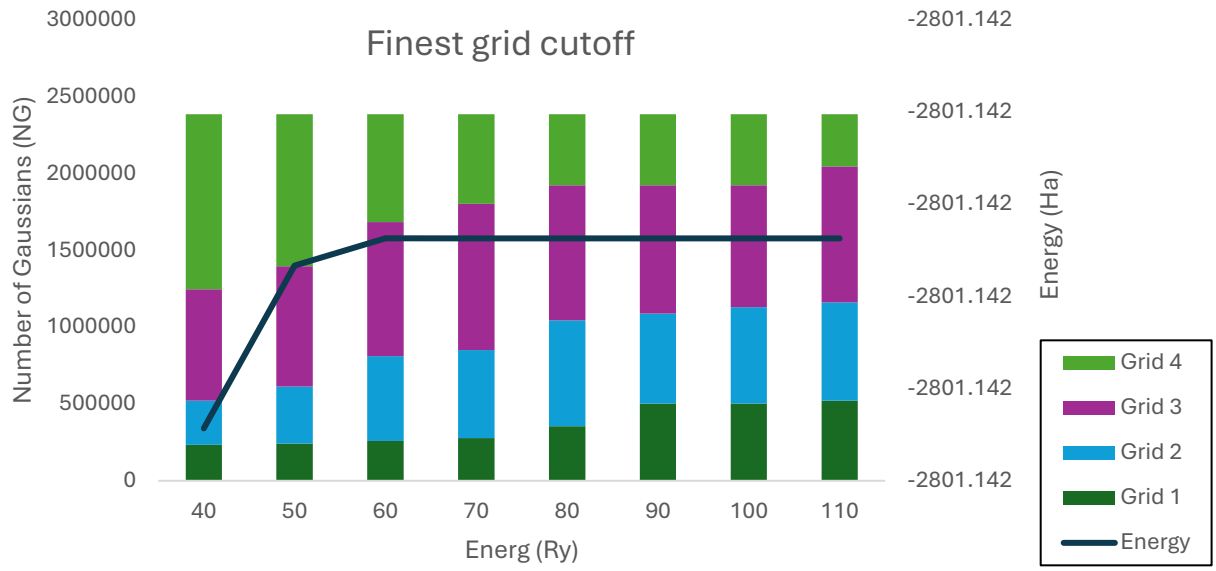

Figure A3. Convergence testing of relative cutoff energies. The number of gaussian functions per grid is shown in the histogram with a line graph depicting the total energy for the system at each relative cutoff energy.

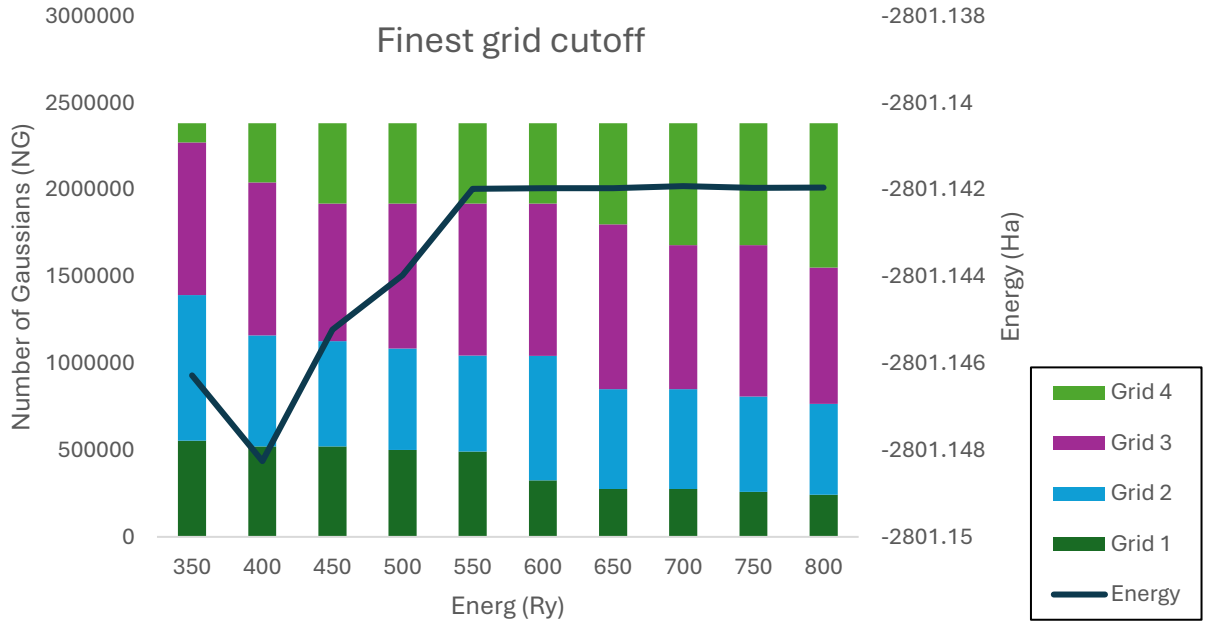

Figure A4. Convergence testing of cutoff energies. The number of gaussian functions per grid is shown in the histogram with a line graph depicting the total energy for the system at each cutoff energy.

APPENDIX 2 – COOLING RATE DETERMINATION

Determining an appropriate cooling rate for the generation of the amorphous structures, through the melt-quench process, is important as it can have a varied effect on the over/under-coordination of sites and the introduction of artifacts, such as large voids. In experimental settings, slow cooling rates can lead to the formation of a crystal structure instead of the desired amorphous one. When using computational methods, however, the timescale required to have a system in a liquid state cool to a crystal structure would likely require multiple months of continuous calculation. Therefore, the main selection criteria for cooling rates becomes ensuring that unnatural artifacts are not introduced and that the system is well converged. In this thesis, four different cooling rates were considered, 100 K/ps, 50 K/ps, 25 K/ps, and 1 K/ps. Ten different models, all containing 224 atoms, were generated for each cooling rate, using the method described in section 2.2.1.

Firstly, in order to gain insights into the effect that cooling rates had on the network coordination, similarly to what was detailed in section 3.2, a cutoff was established via the use of the pair distribution function (equation 3), for each cooling rate, averaged over the 10 models (Figure A5). The left boundary of the first peak and the first peak itself, were found to lie at 1.59 and 1.73 Å, respectively, for all cooling rates. The right peak boundary was found to lie at 2.25, 2.25, 2.29, and 2.19 Å, for systems cooled at 1, 25, 50, and 100 K/ps, respectively, showcasing no discernable trend amongst these. Similarly, the position of the second peak, 2.89, 2.79, 2.78, and 2.82 Å, respectively, showed no correlation between second-neighbor distances and the cooling rates used. Because no major distinguishable pattern had been identified at this point, the average position of the second peak boundary, 2.25 Å was taken as the cutoff distance used for the subsequent analysis of the coordination environment.

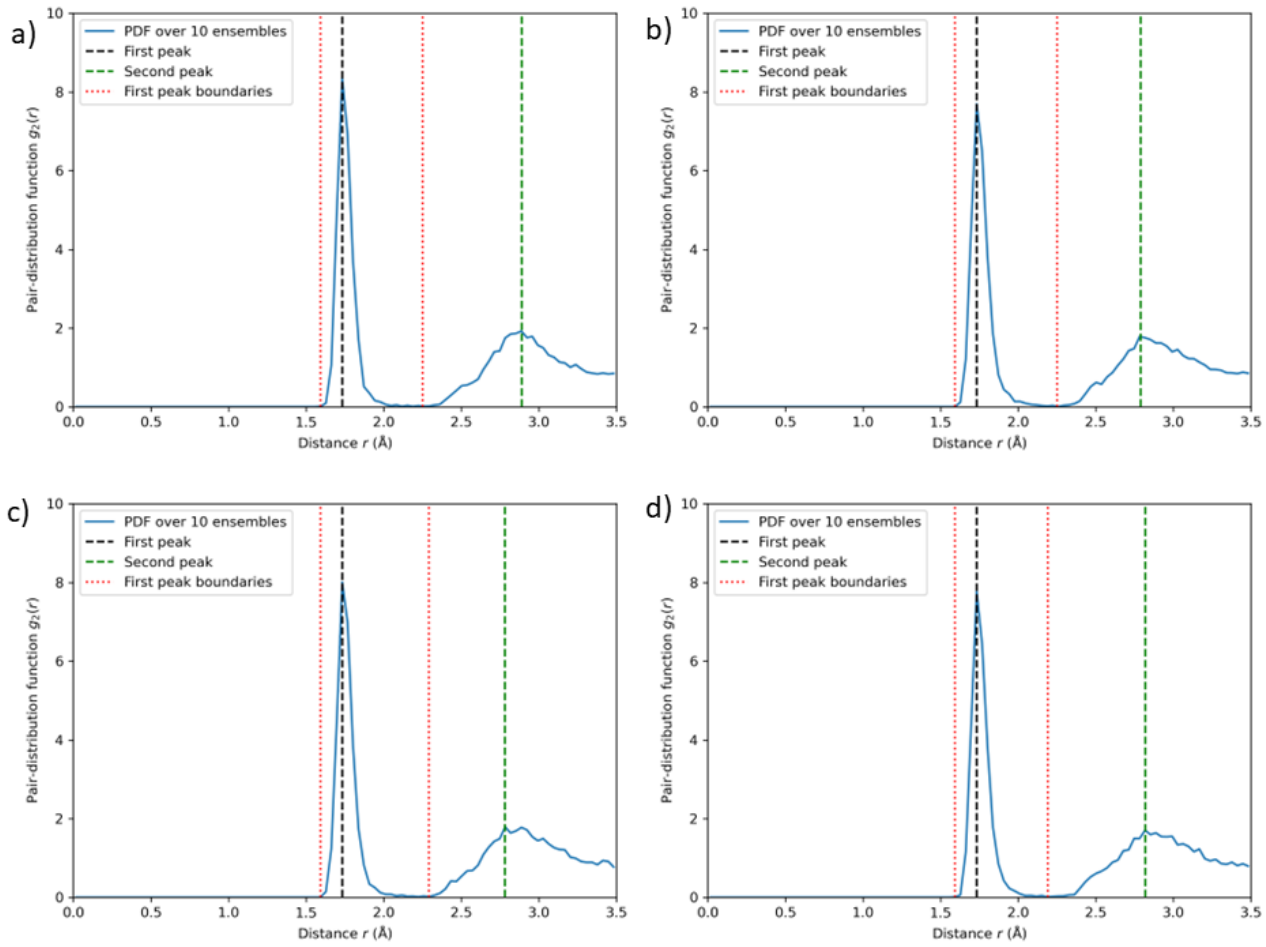

*Figure A5. Pair distribution function averaged over 10 models generated with a cooling rate of **a)** 1K/ps, **b)** 25 K/ps, **c)** 50 K/ps, and **d)** 100 K/ps.*

To assess the difference in network geometry across the different cooling rates, the average Si coordination number, as well as the average bond length was calculated over all 10 models for each cooling rate investigated (Figure A6). The mean bond length of cooling rates 25, 50, and 100 K/ps were found to lie approximately in the same range, with 1K/ps producing the lowest average bond length, and showing the closest agreement with computational literature.[31] A similar trend was seen for the average coordination numbers, where 1 K/ps displayed the best agreement with the literature.[35] Although the expected pattern of increased coordination number (Figure A6) and wider range of pair distances (Figure A5)for faster cooling rates was not observed, the considered cooling rates are likely within too narrow of a range for such a pattern to be discernable. Based on this analysis, 1 K/ps was selected as an appropriate cooling rate for this investigation.

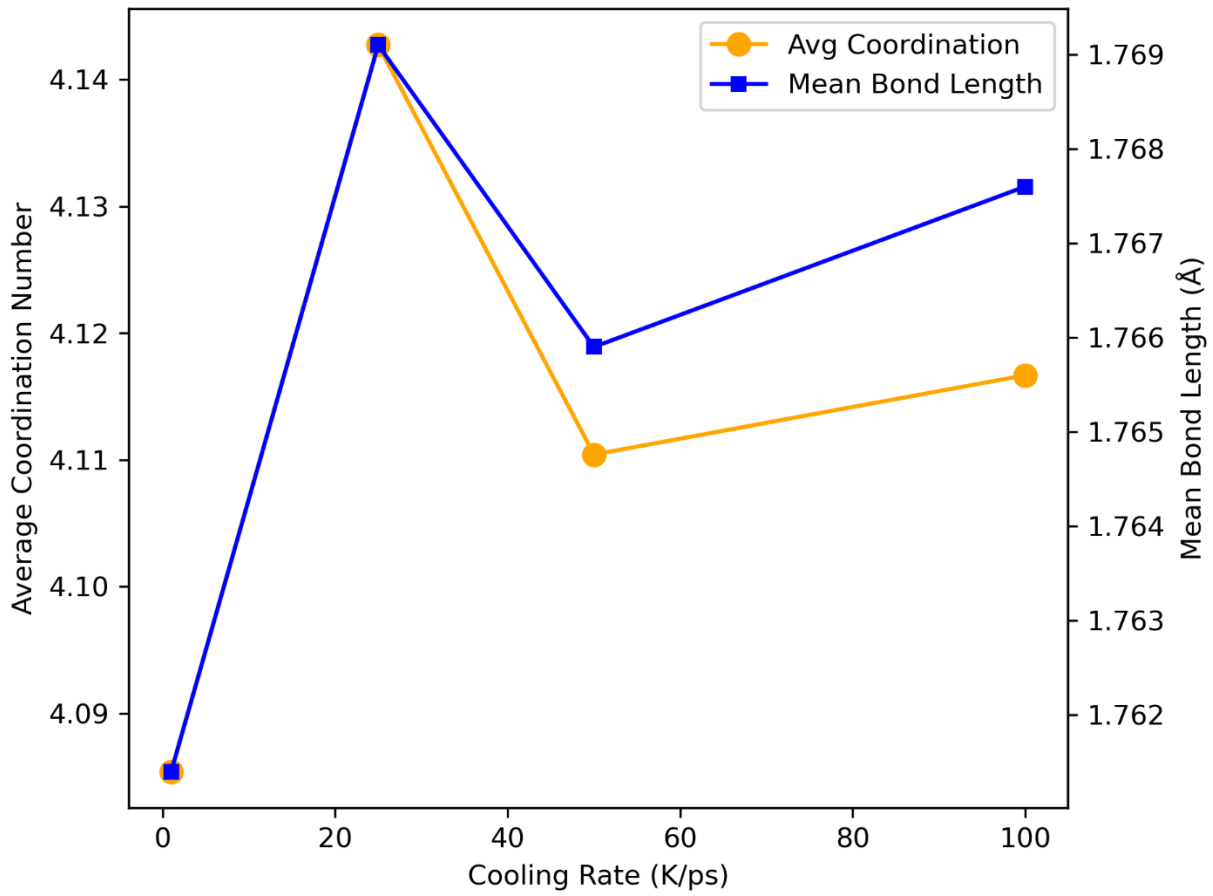

Figure A6.Average coordination number (left axis) and mean bond length in Å within the coordination sphere (right axis), for all four investigated cooling rates, averaged over 10 prepared ensembles.

REFERENCES

(1) Au, H.; Crespo-Ribadeneyra, M.; Titirici, M.-M. Beyond Li-Ion Batteries: Performance, Materials Diversification, and Sustainability. *One Earth* **2022**, *5* (3), 207–211. https://doi.org/10.1016/j.oneear.2022.02.014.

(2) Sankar, T. K.; Abhilash; Meshram, P. Environmental Impact Assessment in the Entire Life Cycle of Lithium-Ion Batteries. *Rev. Environ. Contam. Toxicol.* **2024**, *262* (1), 5. https://doi.org/10.1007/s44169-023-00054-w.

(3) Yoo, H. D.; Markevich, E.; Salitra, G.; Sharon, D.; Aurbach, D. On the Challenge of Developing Advanced Technologies for Electrochemical Energy Storage and Conversion. *Mater. Today* **2014**, *17* (3), 110–121. https://doi.org/10.1016/j.mattod.2014.02.014.

(4) Cottom, J.; Hückmann, L.; Meyer, J.; Olsson, E. Forged by Charge: Polaron-Induced Matrix Formation in Silicon Nitride Conversion-Type Anodes for Lithium-Ion Batteries. *J. Mater. Chem. A* **2025**, *13* (40), 34260–34272. https://doi.org/10.1039/D5TA04013B.

(5) Wang, L.; Światowska, J.; Dai, S.; Cao, M.; Zhong, Z.; Shen, Y.; Wang, M. Promises and Challenges of Alloy-Type and Conversion-Type Anode Materials for Sodium–Ion Batteries. *Mater. Today Energy* **2019**, *11*, 46–60. https://doi.org/10.1016/j.mtener.2018.10.017.

(6) Olsson, E.; Yu, J.; Zhang, H.; Cheng, H.-M.; Cai, Q. Atomic-Scale Design of Anode Materials for Alkali Metal (Li/Na/K)-Ion Batteries: Progress and Perspectives. *Adv. Energy Mater.* **2022**, *12* (25), 2200662. https://doi.org/10.1002/aenm.202200662.

(7) Lovett, A. J.; Füredi, M.; Bird, L.; Said, S.; Frost, B.; Shearing, P. R.; Guldin, S.; Miller, T. S. Structural Evolution of Silicon Nitride Anodes during Electrochemical Lithiation. *ACS Electrochem.* **2025**, *1* (6), 962–973. https://doi.org/10.1021/acselectrochem.4c00230.

(8) Ngoy, K. R.; Lukong, V. T.; Yoro, K. O.; Makambo, J. B.; Chukwuati, N. C.; Ibegbulam, C.; Eterigho-Ikelegbe, O.; Ukoba, K.; Jen, T.-C. Lithium-Ion Batteries and the Future of Sustainable Energy: A Comprehensive Review. *Renew. Sustain. Energy Rev.* **2025**, *223*, 115971. https://doi.org/10.1016/j.rser.2025.115971.

(9) Dell, R. M.; Rand, D. A. J. How a Battery Operates. In *Understanding Batteries*; Dell, R. M., Rand, D. A. J., Connor, P., Bailey, R. (Bob) D., Eds.; The Royal Society of Chemistry, 2001; p 0. https://doi.org/10.1039/9781847552228-00010.

(10) Yabuuchi, N.; Kubota, K.; Dahbi, M.; Komaba, S. Research Development on Sodium-Ion Batteries. *Chem. Rev.* **2014**, *114* (23), 11636–11682. https://doi.org/10.1021/cr500192f.

(11) Dell, R. M.; Rand, D. A. J. How to Choose a Battery. In *Understanding Batteries*; Dell, R. M., Rand, D. A. J., Connor, P., Bailey, R. (Bob) D., Eds.; The Royal Society of Chemistry, 2001; p 0. https://doi.org/10.1039/9781847552228-00022.

(12) Torabi, F.; Ahmadi, P. Chapter 2 - Fundamentals of Batteries. In *Simulation of Battery Systems*; Academic Press, 2020; pp 55–81. https://doi.org/10.1016/B978-0-12-816212-5.00006-4.

(13) Pilali, E.; Nia, F. F.; Yamini, E.; Esmaeilion, F.; Alfraidi, W.; Taklifi, A.; Garcia, D. A.; Soltani, M. SWOT Analysis on the Transition from Lithium-Ion Batteries to Sodium-Ion Batteries. *Sustain. Energy Technol. Assess.* **2025**, *80*, 104371. https://doi.org/10.1016/j.seta.2025.104371.

(14) A. Langevin, S.; A. McHale, C.; Hamann, T.; S. Ko, J. Systematic Design of Safe, High-Energy Lithium-Ion Batteries by Merging Intercalation and Alloying Anodes. *J. Mater. Chem. A* **2025**, *13* (33), 27093–27100. https://doi.org/10.1039/D5TA05287D.

(15) Tareq, F. K.; Rudra, S. Enhancing the Performance of Silicon-Based Anode Materials for Alkali Metal (Li, Na, K) Ion Battery: A Review on Advanced Strategies. *Mater. Today Commun.* **2024**, *39*, 108653. https://doi.org/10.1016/j.mtcomm.2024.108653.

(16) Cheng, H.; Garcia-Araez, N.; L. Hector, A. Enhancing the Performance of Hard Carbon for Sodium-Ion Batteries by Coating with Silicon Nitride/Oxycarbide Nanoparticles. *Mater. Adv.* **2021**, *2* (24), 7956–7966. https://doi.org/10.1039/D1MA00613D.

(17) Ulvestad, A.; Andersen, H. F.; Jensen, I. J. T.; Mongstad, T. T.; Mæhlen, J. P.; Prytz, Ø.; Kirkengen, M. Substoichiometric Silicon Nitride – An Anode Material for Li-Ion Batteries Promising High Stability and High Capacity. *Sci. Rep.* **2018**, *8* (1), 8634. https://doi.org/10.1038/s41598-018-26769-8.
(18) Xie, J.; Lu, Y.-C. A Retrospective on Lithium-Ion Batteries. *Nat. Commun.* **2020**, *11* (1), 2499. https://doi.org/10.1038/s41467-020-16259-9.
(19) Teng, W.; Wu, J.; Liang, Q.; Deng, J.; Xu, Y.; Liu, Q.; Wang, B.; Ma, T.; Nan, D.; Liu, J.; Li, B.; Weng, Q.; Yu, X. Designing Advanced Liquid Electrolytes for Alkali Metal Batteries: Principles, Progress, and Perspectives. *ENERGY Environ. Mater.* **2023**, *6* (2), e12355. https://doi.org/10.1002/eem2.12355.
(20) Yu, X.; Chen, S.; Tang, B.; Li, X.-L.; Zhou, J.; Ren, Y.; Wei, J.; Yang, C.; Guo, Y.; Zhou, Z.; Bo, S.-H. The Debate over Hard Carbon and Alloy Anodes Continues for Solid-State Sodium Batteries. *ACS Energy Lett.* **2024**, *9* (9), 4441–4449. https://doi.org/10.1021/acsenergylett.4c01686.
(21) Zuo, W.; Liu, Z.; Dopilka, A.; Yang, Z.; Li, Y.; Kubal, J.; Kim, H.; Liu, F.; Liu, P.; Ngo, A. T.; Nelson Weker, J.; Chen, Z.; Kostecki, R.; Wulf-Knoerzer, J.; Srinivasan, V.; Cui, Y.; Amine, K.; Xu, G.-L. Next-Generation Anodes for High-Energy and Low-Cost Sodium-Ion Batteries. *Nat. Rev. Mater.* **2026**, *11* (2), 117–135. https://doi.org/10.1038/s41578-025-00857-4.
(22) Saju, S. K.; Chattopadhyay, S.; Xu, J.; Alhashim, S.; Pramanik, A.; Ajayan, P. M. Hard Carbon Anode for Lithium-, Sodium-, and Potassium-Ion Batteries: Advancement and Future Perspective. *Cell Rep. Phys. Sci.* **2024**, *5* (3), 101851. https://doi.org/10.1016/j.xcrp.2024.101851.
(23) Jian, Z.; Bommier, C.; Luo, L.; Li, Z.; Wang, W.; Wang, C.; Greaney, P. A.; Ji, X. Insights on the Mechanism of Na-Ion Storage in Soft Carbon Anode. *Chem. Mater.* **2017**, *29* (5), 2314–2320. https://doi.org/10.1021/acs.chemmater.6b05474.
(24) Ge, P.; Fouletier, M. Electrochemical Intercalation of Sodium in Graphite. *Solid State Ion.* **1988**, *28–30*, 1172–1175. https://doi.org/10.1016/0167-2738(88)90351-7.
(25) Xu, H.; Li, H.; Wang, X. The Anode Materials for Lithium-Ion and Sodium-Ion Batteries Based on Conversion Reactions: A Review. *ChemElectroChem* **2023**, *10* (9), e202201151. https://doi.org/10.1002/celc.202201151.
(26) Huggins, R. A. Alternative Materials for Negative Electrodes in Lithium Systems. *Solid State Ion.* **2002**, *152–153*, 61–68. https://doi.org/10.1016/S0167-2738(02)00337-5.
(27) Idota, Y.; Kubota, T.; Matsufuji, A.; Maekawa, Y.; Miyasaka, T. Tin-Based Amorphous Oxide: A High-Capacity Lithium-Ion-Storage Material. *Science* **1997**, *276* (5317), 1395–1397. https://doi.org/10.1126/science.276.5317.1395.
(28) Ulvestad, A.; Andersen, H. F.; Mæhlen, J. P.; Prytz, Ø.; Kirkengen, M. Long-Term Cyclability of Substoichiometric Silicon Nitride Thin Film Anodes for Li-Ion Batteries. *Sci. Rep.* **2017**, *7* (1), 13315. https://doi.org/10.1038/s41598-017-13699-0.
(29) Ulvestad, A.; Mæhlen, J. P.; Kirkengen, M. Silicon Nitride as Anode Material for Li-Ion Batteries: Understanding the SiNx Conversion Reaction. *J. Power Sources* **2018**, *399*, 414–421. https://doi.org/10.1016/j.jpowsour.2018.07.109.
(30) Sarki, M. U.; Echi, I. M.; Amah, A. N.; Ahemen, I.; Chan, K. T.; Rilwan, U.; Sayyed, M. I. Structural, Electronic and Optical Properties of α -Si3N4, β-Si3N4 and γ-Si3N4 Using Density Functional Theory. *Res.* **2024**, *1* (2), 100048. https://doi.org/10.1016/j.nexres.2024.100048.
(31) Vedula, R. P. Effect of Topological Disorder on Structural, Mechanical, and Electronic Properties of Amorphous Silicon Nitride: An Atomistic Study. *Phys. Rev. B* **2012**, *85* (20). https://doi.org/10.1103/PhysRevB.85.205209.
(32) Martín-Gil, M.; Rabanal, M. E.; Várez, A.; Kuhn, A.; García-Alvarado, F. Mechanical Grinding of Si3N4 to Be Used as an Electrode in Lithium Batteries. *Mater. Lett.* **2003**, *57* (20), 3063–3069. https://doi.org/10.1016/S0167-577X(02)01437-4.
(33) Ramar, A.; Sanjana, K.; Wang, F.-M. Carbides and Nitrides: Advanced Materials for Engineering the Electrochemistry of Silicon Anodes for High Energy Density Lithium-Ion Battery. *Chem. Eng. J.* **2024**, *491*, 151921. https://doi.org/10.1016/j.cej.2024.151921.
(34) Zhao, Y.-N.; Chen, K.-A.; Han, L.-X.; Ma, M.-M.; Li, H.; Ai, X.-P.; Fang, Y.-J.; Cao, Y.-L. Structural Transformation from Crystalline to Amorphous States to Boost Sodium Storage Properties of

NaVOPO4 Cathode. *Rare Met.* **2025**, *44* (10), 7230–7241. https://doi.org/10.1007/s12598-025-03407-7.
(35) Hückmann, L.; Cottom, J.; Meyer, J. Intrinsic Charge Trapping and Reversible Charge Induced Structural Modifications in A-Si3N4. *Adv. Phys. Res.* **2024**, *3* (2), 2300109. https://doi.org/10.1002/apxr.202300109.
(36) Lin, S.-Y. Electronic Defect States of Amorphous Silicon Nitride. *Opt. Mater.* **2003**, *23* (1), 93–98. https://doi.org/10.1016/S0925-3467(03)00066-1.
(37) Kroll, P. The Electronic Structure and Other Properties of Amorphous Silicon Nitride Investigated with Density Functional Theory. *MRS Online Proc. Libr.* **2011**, *715* (1), 101. https://doi.org/10.1557/PROC-715-A10.1.
(38) Ching, W. Y.; Ouyang, L.; Gale, J. D. Full *Ab Initio* Geometry Optimization of All Known Crystalline Phases of Si 3 N 4. *Phys. Rev. B* **2000**, *61* (13), 8696–8700. https://doi.org/10.1103/PhysRevB.61.8696.
(39) Nemaga, A. W.; Lai, S. Y.; Abdelhamid, M.; Koposov, A.; Mæhlen, J. P.; Andersen, H. F.; Ulvestad, A. In-Situ Convertible Amorphous Silicon Nitride (SiNx) Anode: Resolving the Long-Term Cyclic Instability of Silicon. *ECS Meet. Abstr.* **2023**, *MA2023-02* (2), 243. https://doi.org/10.1149/MA2023-022243mtgabs.
(40) Ulvestad, A.; Mæhlen, J. P.; Kirkengen, M. Silicon Nitride as Anode Material for Li-Ion Batteries: Understanding the SiNx Conversion Reaction. *J. Power Sources* **2018**, *399*, 414–421. https://doi.org/10.1016/j.jpowsour.2018.07.109.
(41) Damircheli, R.; Hoang, B.; Ferrari, V. C.; Lin, C.-F. Highly Uniform Nitride-Rich Artificial Solid Electrolyte Interphase Enabled by Nano-Silicon Nitride for Superior Performance in Advanced Sodium Metal Batteries. *J. Mater. Chem. A* **2024**, *12* (46), 31949–31958. https://doi.org/10.1039/D4TA05595K.
(42) Franco, A. A. Multiscale Modelling and Numerical Simulation of Rechargeable Lithium Ion Batteries: Concepts, Methods and Challenges. *RSC Adv.* **2013**, *3* (32), 13027–13058. https://doi.org/10.1039/C3RA23502E.
(43) Marzari, N.; Ferretti, A.; Wolverton, C. Electronic-Structure Methods for Materials Design. *Nat. Mater.* **2021**, *20* (6), 736–749. https://doi.org/10.1038/s41563-021-01013-3.
(44) Yang, X.; Li, Y.; Liu, Y.; Li, Q.; Yang, T.; Jia, H. Crystal Structure Prediction and Performance Assessment of Hydrogen Storage Materials: Insights from Computational Materials Science. *Energies* **2024**, *17* (14), 3591. https://doi.org/10.3390/en17143591.
(45) Hasnip, P. J.; Refson, K.; Probert, M. I. J.; Yates, J. R.; Clark, S. J.; Pickard, C. J. Density Functional Theory in the Solid State. *Philos. Transact. A Math. Phys. Eng. Sci.* **2014**, *372* (2011), 20130270. https://doi.org/10.1098/rsta.2013.0270.
(46) Sholl, D. S.; Steckel, J. A. *Density Functional Theory: A Practical Introduction*; John Wiley & Sons, Inc., 2009.
(47) Jensen, F. *Introduction to Computational Chemistry*, 2nd ed.; John Wiley & Sons Ltd, 2007.
(48) Christie, J. K. Review: Understanding the Properties of Amorphous Materials with High-Performance Computing Methods. *Philos. Trans. R. Soc. Math. Phys. Eng. Sci.* **2023**, *381* (2250), 20220251. https://doi.org/10.1098/rsta.2022.0251.
(49) Olsson, E. I. K. Computational Modelling of SmCoO3-Based Cathode Materials for Solid Oxide Fuel Cells. Doctoral, UCL (University College London), 2017, pp 1–238. https://discovery.ucl.ac.uk/id/eprint/1572244/ (accessed 2026-05-16).
(50) Islam, M. S.; Fisher, C. A. J. Lithium and Sodium Battery Cathode Materials: Computational Insights into Voltage, Diffusion and Nanostructural Properties. *Chem. Soc. Rev.* **2013**, *43* (1), 185–204. https://doi.org/10.1039/C3CS60199D.
(51) *VESTA 3.5.7 – 3D Visualization System for Electronic & Structural Analysis – My Biosoftware – Bioinformatics Softwares Blog*. https://mybiosoftware.com/vesta-3d-visualization-system-electronic-structural-analysis.html (accessed 2026-05-17).
(52) Humphrey, W.; Dalke, A.; Schulten, K. VMD: Visual Molecular Dynamics. *J. Mol. Graph.* **1996**, *14* (1), 33–38. https://doi.org/10.1016/0263-7855(96)00018-5.

(53) *CP2K: An electronic structure and molecular dynamics software package - Quickstep: Efficient and accurate electronic structure calculations | The Journal of Chemical Physics | AIP Publishing*. https://pubs.aip.org/aip/jcp/article/152/19/194103/199081/CP2K-An-electronic-structure-and-molecular (accessed 2026-03-04).
(54) VandeVondele, J.; Hutter, J. Gaussian Basis Sets for Accurate Calculations on Molecular Systems in Gas and Condensed Phases. *J. Chem. Phys.* **2007**, *127* (11), 114105. https://doi.org/10.1063/1.2770708.
(55) Hartwigsen, C.; Goedecker, S.; Hutter, J. Relativistic Separable Dual-Space Gaussian Pseudopotentials from H to Rn. *Phys. Rev. B* **1998**, *58* (7), 3641–3662. https://doi.org/10.1103/PhysRevB.58.3641.
(56) Goedecker, S.; Teter, M.; Hutter, J. Separable Dual-Space Gaussian Pseudopotentials. *Phys. Rev. B* **1996**, *54* (3), 1703–1710. https://doi.org/10.1103/PhysRevB.54.1703.
(57) Krack, M. Pseudopotentials for H to Kr Optimized for Gradient-Corrected Exchange-Correlation Functionals. *Theor. Chem. Acc.* **2005**, *114* (1), 145–152. https://doi.org/10.1007/s00214-005-0655-y.
(58) Fletcher, R. A New Approach to Variable Metric Algorithms. *Comput. J.* **1970**, *13* (3), 317–322. https://doi.org/10.1093/comjnl/13.3.317.
(59) Perdew, J. P.; Burke, K.; Ernzerhof, M. Generalized Gradient Approximation Made Simple. *Phys. Rev. Lett.* **1996**, *77* (18), 3865–3868. https://doi.org/10.1103/PhysRevLett.77.3865.
(60) Heyd, J.; Scuseria, G. E.; Ernzerhof, M. Hybrid Functionals Based on a Screened Coulomb Potential. *J. Chem. Phys.* **2003**, *118* (18), 8207–8215. https://doi.org/10.1063/1.1564060.
(61) Heyd, J.; Scuseria, G. E.; Ernzerhof, M. Erratum: "Hybrid Functionals Based on a Screened Coulomb Potential" [J. Chem. Phys. 118, 8207 (2003)]. *J. Chem. Phys.* **2006**, *124* (21), 219906. https://doi.org/10.1063/1.2204597.
(62) Anthony R., W. *Solid State Chemistry and Its Applications*, 2nd ed.; 2014.
(63) Cottom, J.; Hückmann, L.; Olsson, E.; Meyer, J. From Jekyll to Hyde and Beyond: Hydrogen's Multifaceted Role in Passivation, H-Induced Breakdown, and Charging of Amorphous Silicon Nitride. *J. Phys. Chem. Lett.* **2024**, *15* (3), 840–848. https://doi.org/10.1021/acs.jpclett.3c03376.
(64) Singh, S.; Chandra, S. Developing Atomistic Glass Models Using Potential-Free Monte Carlo Method: From Simple to Complex Structures. *Comput. Mater. Sci.* **2022**, *202*, 110943. https://doi.org/10.1016/j.commatsci.2021.110943.
(65) Anantharaman, T. R.; Suryanarayana, C. Review: A Decade of Quenching from the Melt. *J. Mater. Sci.* **1971**, *6* (8), 1111–1135. https://doi.org/10.1007/BF00980610.
(66) Thompson, A. P.; Aktulga, H. M.; Berger, R.; Bolintineanu, D. S.; Brown, W. M.; Crozier, P. S.; in 't Veld, P. J.; Kohlmeyer, A.; Moore, S. G.; Nguyen, T. D.; Shan, R.; Stevens, M. J.; Tranchida, J.; Trott, C.; Plimpton, S. J. LAMMPS - a Flexible Simulation Tool for Particle-Based Materials Modeling at the Atomic, Meso, and Continuum Scales. *Comput. Phys. Commun.* **2022**, *271*, 108171. https://doi.org/10.1016/j.cpc.2021.108171.
(67) Marian, C. M.; Gastreich, M.; Gale, J. D. Empirical Two-Body Potential for Solid Silicon Nitride, Boron Nitride, and Borosilazane Modifications. *Phys. Rev. B* **2000**, *62* (5), 3117–3124. https://doi.org/10.1103/PhysRevB.62.3117.
(68) Zhang, S. B.; Northrup, J. E. Chemical Potential Dependence of Defect Formation Energies in GaAs: Application to Ga Self-Diffusion. *Phys. Rev. Lett.* **1991**, *67* (17), 2339–2342. https://doi.org/10.1103/PhysRevLett.67.2339.
(69) Maroulis, G. Bonding and (Hyper)Polarizability in the Sodium Dimer. *J. Chem. Phys.* **2004**, *121* (21), 10519–10524. https://doi.org/10.1063/1.1812737.
(70) Okorie, U. S.; Rampho, G. J. Theoretical Computation of Thermodynamic Functions of Sodium Dimer with Modified Shifted Morse Potential. *Comput. Theor. Chem.* **2024**, *1241*, 114925. https://doi.org/10.1016/j.comptc.2024.114925.
(71) Kermode, J.; Pastewka, L.; et al. *Pair-distribution function*. https://libatoms.github.io/matscipy/tools/pair_distribution.html.
(72) Aiyama, T.; Fukunaga, T.; Niihara, K.; Hirai, T.; Suzuki, K. An X-Ray Diffraction Study of the Amorphous Structure of Chemically Vapor-Deposited Silicon Nitride. *J. Non-Cryst. Solids* **1979**, *33* (2), 131–139. https://doi.org/10.1016/0022-3093(79)90043-7.

(73) Burrough, P. A.; McDonnell, R.; Lloyd, C. D. Spatial Analysis Using Continuous Fields. In *Principles of Geographical Information Systems*; 2015.
(74) Ramasubramani, V.; Dice, B. D.; Harper, E. S.; Spellings, M. P.; Anderson, J. A.; Glotzer, S. C. Freud: A Software Suite for High Throughput Analysis of Particle Simulation Data. *Comput. Phys. Commun.* **2020**, *254*, 107275. https://doi.org/10.1016/j.cpc.2020.107275.
(75) Zhang, G.; Hu, H.; Wu, J. Advances in Amorphous Nanomaterials: Synthesis, Characterization and Application. *Mater. Today Nano* **2025**, *32*, 100675. https://doi.org/10.1016/j.mtnano.2025.100675.
(76) VandeVondele, J.; Hutter, J. Gaussian Basis Sets for Accurate Calculations on Molecular Systems in Gas and Condensed Phases. *J. Chem. Phys.* **2007**, *127* (11), 114105. https://doi.org/10.1063/1.2770708.
(77) *Gaussian Plane Wave — CP2K documentation*. https://manual.cp2k.org/trunk/methods/dft/gpw.html (accessed 2026-05-10).
(78) Sarki, M. U.; Echi, I. M.; Amah, A. N.; Ahemen, I.; Chan, K. T.; Rilwan, U.; Sayyed, M. I. Structural, Electronic and Optical Properties of α -Si3N4, β-Si3N4 and γ-Si3N4 Using Density Functional Theory. *Res.* **2024**, *1* (2), 100048. https://doi.org/10.1016/j.nexres.2024.100048.
(79) Tao, S. X.; Theulings, A. M. M. G.; Prodanović, V.; Smedley, J.; Van der Graaf, H. Optical Properties of Silicon-Rich Silicon Nitride (SixNyHz) from First Principles. *Computation* **2015**, *3* (4), 657–669. https://doi.org/10.3390/computation3040657.
(80) *How to Converge the CUTOFF and REL_CUTOFF — CP2K documentation*. https://manual.cp2k.org/trunk/methods/dft/cutoff.html (accessed 2026-05-10).